Ether lipids influence cancer cell fate by modulating iron uptake

Ryan P. Mansell[1,2,#], Sebastian Müller[3,#], Jia-Shu Yang[4], Sarah Innes-Gold[5], Sunny Das[6], Ferenc Reinhardt[6], Kim Janina Sigmund[6], Vaishnavi V. Phadnis[1,6], Zhengpeng Wan[7], Jillian Stark[1,2], Daehee Hwang[1,2], Fabien Sindikubwabo[3], Laurène Syx[8], Nicolas Servant[8], Elinor Ng Eaton[6], Julio L. Sampaio[9], George W. Bell[6], Prathapan Thiru[6], Amartya Viravalli[10], Amy Deik[11], Clary B. Clish[11], Paula T. Hammond[2,12], Roger D. Kamm[7,13], Adam E. Cohen[5,14], Ilya Levental[15], Natalie Boehnke[10], Victor W. Hsu[4], Kandice R. Levental[15], Raphaël Rodriguez[3,*], Robert A. Weinberg[1,6,16,*], and Whitney S. Henry[1,2,*,§]

1. Dept. of Biology, MIT, Cambridge, MA 02139, USA
2. Koch Institute for Integrative Cancer Research, MIT, Cambridge, MA 02139, USA
3. Institut Curie, CNRS, INSERM, PSL Research University, Equipe Labellisée Ligue Contre le Cancer, Paris 75005, France
4. Division of Rheumatology, Inflammation and Immunity, Brigham and Women's Hospital, and Dept. of Medicine, Harvard Medical School, Boston, MA 02115, USA
5. Dept. of Chemistry and Chemical Biology, Harvard University, Cambridge, MA 02138, USA
6. Whitehead Institute for Biomedical Research, Cambridge, MA 02142, USA
7. Dept. of Biological Engineering, MIT, Cambridge, MA 02139, USA
8. Institut Curie, INSERM, Mines ParisTech, Paris 75005, France
9. Institut Curie, CurieCoreTech Metabolomics and Lipidomics platform, Paris 75005, France
10. Dept. of Chemical Engineering and Materials Science, University of Minnesota Minneapolis, MN 55455, USA
11. The Broad Institute of MIT and Harvard, Cambridge, MA 02142, USA
12. Dept. of Chemical Engineering, MIT, Cambridge, MA 02139, USA
13. Dept. of Mechanical Engineering, MIT, Cambridge, MA 02139, USA
14. Dept. of Physics, Harvard University, Cambridge, MA 02138, USA
15. Dept. of Molecular Physiology and Biological Physics, Center for Membrane and Cell Physiology, University of Virginia, Charlottesville, VA 22903, USA
16. Ludwig Center for Molecular Oncology, Cambridge, MA 02139, USA

[#]These authors contributed equally
[§]Lead contact
*Correspondence: Raphaël Rodriguez, PhD (raphael.rodriguez@curie.fr), Robert A. Weinberg, PhD (weinberg@wi.mit.edu) and Whitney S. Henry (wshenry@mit.edu)

ABSTRACT

Cancer cell fate has been widely ascribed to mutational changes within protein-coding genes associated with tumor suppressors and oncogenes. In contrast, the mechanisms through which the biophysical properties of membrane lipids influence cancer cell survival, dedifferentiation and metastasis have received little scrutiny. Here, we report that cancer cells endowed with high metastatic ability and cancer stem cell-like traits employ ether lipids to maintain low membrane tension and high membrane fluidity. Using genetic approaches and lipid reconstitution assays, we show that these ether lipid-regulated biophysical properties permit non-clathrin-mediated iron endocytosis via CD44, resulting in significant increases in intracellular redox-active iron and enhanced ferroptosis susceptibility. Using a combination of in vitro three-dimensional microvascular network systems and in vivo animal models, we show that loss of ether lipids from plasma membranes also strongly attenuates extravasation, metastatic burden and cancer stemness. These findings illuminate a mechanism whereby ether lipids in carcinoma cells serve as key regulators of malignant progression while conferring a unique vulnerability that can be exploited for therapeutic intervention.

KEYWORDS

Ether lipids, membrane tension, endocytosis, CD44, iron, metastasis, ferroptosis.

INTRODUCTION

Cancer cells have the capacity to undergo dynamic changes in identity, structure, and function, making them remarkably versatile and adaptable. Alterations in the lipid composition of cell membranes contribute to the phenotypic plasticity of cells. The distinctive physicochemical properties and subcellular localization of various lipids within cell membranes influence a range of biological processes, including cellular trafficking, signaling and metabolism[1]. Despite growing knowledge of lipid biology, an understanding of how specific lipid subtypes impact cancer cell fate remains limited.

Emerging studies demonstrate that therapy-resistant mesenchymal-like carcinoma cells exhibit an elevated vulnerability to ferroptosis[2-4], an iron-dependent form of cell death characterized by an unrestricted accumulation of oxidized membrane phospholipids[5-8]. In previous work we showed that the natural product salinomycin can selectively eliminate otherwise therapy-resistant, mesenchymal-enriched cancer stem cells (CSC) by targeting lysosomal iron to promote an iron-dependent cell death[4, 9, 10]. In this context, we found that such CSC-enriched cells exhibit a high intracellular iron load compared to their non-CSC-like counterparts, rendering them especially vulnerable to elimination by induced ferroptosis[4].

Ferroptosis can also be instigated by pharmacologic inhibition of ferroptosis suppressors, such as glutathione peroxidase 4 (GPX4)[5, 11], ferroptosis-suppressor protein 1 (FSP1, previously known as AIFM2)[12, 13], as well as through downregulation of reduced glutathione (GSH)[14, 15]. Activated $CD8^+$ T cells may also induce ferroptosis in cancer cells[16, 17]. Beyond cancer, ferroptosis has been implicated in the pathogenesis of several neurodegenerative diseases and acute injury of the kidney, liver and heart[18-21].

In previous work, we undertook an unbiased, genome-wide CRISPR/Cas9 screen with the goal of identifying genes that govern ferroptosis susceptibility in high-grade human serous ovarian cancer cells[22]. This screen revealed a previously unrecognized role for ether lipid-synthesizing enzymes, such as alkylglycerone phosphate synthase (AGPS), in modulating ferroptosis susceptibility. The ether phospholipids generated by these enzymes represent a unique subclass of glycerophospholipids characterized by an ether-linked hydrocarbon group formed at the *sn*-1 position of the glycerol backbone[23]. This phospholipid subtype constitutes ~20% of the total phospholipid pool in many types of mammalian cells.

The significance of ether lipid species in human health is underscored by the severe inherited peroxisomal disorders caused by their deficiency[23]. This often manifests as profound developmental abnormalities, such as neurological defects, vision and hearing loss, and reduced lifespan. In the context of cancer, elevated ether lipid levels have been correlated with increased metastatic potential of carcinoma cells[24-27]. Despite these pathological associations, the mechanism(s) by which ether lipids affect cancer progression remain(s) elusive. Furthermore, the mechanism(s) by which loss of ether lipids results in decreased ferroptosis susceptibility required further investigation.

Our previous work, along with that of others, ascribed a role to polyunsaturated ether phospholipids as chemical substrates prone to the iron-mediated oxidation that triggers ferroptotic cell death[22, 28]. Here, we demonstrate that ether lipids also play an unrelated biophysical role, facilitating iron endocytosis in carcinoma cells. This represents an unappreciated mechanism of intracellular signaling by which ether lipids contribute to intracellular levels of a critical metal catalyst. In addition, our findings highlight the functional importance of this poorly studied lipid subtype in enabling a variety of malignancy-associated cell phenotypes, including metastasis and tumor-initiating abilities. Taken together, these results establish a role for ether lipids as critical effectors of cancer cell fate.

RESULTS

Ether lipids play a key role in maintaining a ferroptosis-susceptible cell state

To investigate the mechanism(s) by which ether lipid deficiency reduces ferroptosis susceptibility, we employed CRISPR/Cas9 to knockout (KO) the *AGPS* gene in ferroptosis-sensitive TGF-β-treated PyMT-1099 murine breast carcinoma cancer cells[29] **(Extended Data Fig. 1a).** The *AGPS* gene encodes a rate-limiting enzyme critical for ether lipid biosynthesis[23] **(Fig. 1a)**. Consistent with our prior studies[22], loss of ether lipids via AGPS KO significantly decreased the susceptibility of these cancer cells to ferroptosis induced by treatment with the GPX4 inhibitors RSL3 or ML210 **(Fig. 1b, Extended Data Fig. 1b).**

Lipidomic analysis confirmed that *AGPS* knockout significantly reduces total ether lipid abundance, while only marginally affecting most other membrane-associated lipid species **(Fig. 1c, Extended Data Fig. 2a)**. More than half of the identified ether lipids contained polyunsaturated fatty acyl groups, which are highly prone to hydrogen abstraction by reactive free radicals **(Fig. 1d)**. Based on this observation, we speculated that loss of ether lipids may attenuate ferroptosis susceptibility by depleting the pool of

available ether lipid substrates for lipid peroxidation. Thus, we performed oxidized lipidomic analysis on two ferroptosis-sensitive breast cancer cell lines treated with either ML210 or RSL3. These experiments confirmed that ether lipids are oxidized following ferroptosis induction **(Fig. 1e, Extended Data Fig. 1c)**.

In order to test whether ether lipid deficiency leads to a global reduction of cellular pools of oxidation prone lipid species, we also investigated whether the relative abundance of pro-ferroptosis non-ether-linked polyunsaturated phospholipids was impacted by loss of ether lipids. Our analyses revealed that while total levels of phospholipid unsaturation are only marginally changed, ether lipid deficiency increased the relative abundance of several polyunsaturated diacyl phosphoethanolamine (PE) and phosphatidylcholine (PC)-derived lipids with putative pro-ferroptosis function[30, 31] **(Fig. 1f, Extended Data Fig. 2b-d)**. To ensure that these findings were not an idiosyncrasy of our TGF-β-treated PyMT-1099 AGPS KO cells, we confirmed this observation in PyMT-MMTV-derived pB3 murine AGPS KO breast carcinoma cells[32] **(Fig. 1g, 1h, Extended Data Fig. 1d, 3a-3f)**. Importantly, re-expression of AGPS (addback) restored the relative levels of these non-ether-linked polyunsaturated diacyl phospholipids to levels comparable to pB3 wildtype (WT) cells **(Fig. 1i)**. These findings dispel the notion that ether lipid deficiency attenuates ferroptosis susceptibility simply by decreasing the global level of polyunsaturated phospholipids, further underscoring the importance of polyunsaturated ether phospholipids in maintaining a ferroptosis susceptible cell state.

Ether lipids regulate levels of cellular redox-active iron in cancer cells

The above observations, together with our oxidized ether phospholipidomic analysis, supported the notion that ether lipids could modulate ferroptosis susceptibility— at least in part by serving as substrates for lipid peroxidation. However, these observations failed to address the possibility that alterations in ether lipid composition could also affect intracellular levels of redox-active iron, the central mediator of the lipid peroxidation that drives ferroptosis. Therefore, we used two orthogonal analyses to assess intracellular iron levels. Since the endolysosomal compartment is a key reservoir of reactive iron within cells[7, 33-35], we used a lysosomal iron (II)-specific fluorescent probe, HRhoNox-M[36], to gauge levels of lysosomal redox active iron. In addition, we used inductively coupled plasma mass spectrometry (ICP-MS) to quantify total intracellular iron levels[7, 35, 37-39].

Unexpectedly, loss of ether lipids (via AGPS KO) reduced intracellular iron levels in all murine cancer cell lines tested, whereas AGPS addback restored intracellular iron to levels comparable to those seen in parental ferroptosis-sensitive cancer cells **(Fig. 2a-2d, Extended Data Fig. 4a)**. These findings provided the first indication that changes in ether phospholipids directly affect the levels of intracellular iron. Indeed, there was no direct precedent for the ability of a membrane-associated phospholipid to serve as a key regulator of the levels of an intracellular metal ion.

Supporting these findings, we found that the depletion of ether lipids, achieved via knockout of the fatty acid reductase 1 (FAR1) enzyme[23] **(Extended Data Fig. 4b)**, also resulted in a significant decrease in intracellular iron levels, in this case in the OVCAR8 human high-grade serous ovarian cancer cell line, which exhibits mesenchymal characteristics[40] **(Fig. 2e, 2f).** Furthermore, we noted that treatment of

AGPS KO cells with ferric ammonium citrate (FAC)[41, 42], which provides an exogenous source of ferric ions, re-sensitized cultured AGPS KO mesenchymal breast and ovarian carcinoma cells to ferroptosis induction (that could be rescued by the ferroptosis inhibitor liproxstatin-1), doing so even in the absence of elevated ether phospholipids **(Fig. 2g, 2h)**.

We further extended this analysis by studying the behavior of mammary carcinoma tumors in vivo. Consistent with our in vitro data, ICP-MS indicated that total iron levels are reduced in breast tumors derived from implanted pB3 AGPS KO cells relative to those arising from either pB3 WT or pB3 AGPS addback cells **(Fig. 2i)**. These observations reinforced the notion that ether lipids are critical regulators of intracellular iron levels, a rate-limiting component of ferroptosis[7].

Ether lipids facilitate CD44-mediated iron endocytosis

We proceeded to investigate the mechanism(s) by which membrane-associated ether lipids could regulate intracellular iron levels. This led us to examine the behavior of two proteins that are known to act as major mediators of cellular iron import—transferrin receptor 1 (TfR1)[43] and CD44[35]—and whether their functioning was altered in response to loss of ether phospholipids. While CD44 is best known as a cell-surface cancer stem-cell marker[44, 45], recent research has revealed its critical role in mediating endocytosis of iron-bound hyaluronates in CSC-enriched cancer cells and in activated immune cells[35, 39]. To monitor these two alternative iron import mechanisms, we performed endocytosis kinetics experiments using fluorescently labeled transferrin as a proxy for TfR1 internalization and fluorescently labeled hyaluronic acid (HA)—whose main plasma membrane receptor is CD44—as a marker for CD44 internalization[46, 47].

We observed that the rate of TfR1 endocytosis was marginally affected by ether lipid deficiency in pB3 cells **(Fig. 3a, Extended Data Fig. 5a)**. In stark contrast, CD44-mediated endocytosis was significantly impaired in these ether lipid-deficient cancer cells **(Fig. 3b, Extended Data Fig. 5b)**. Conversely, CD44-dependent iron import in AGPS KO cells could be restored to WT levels upon AGPS addback **(Fig. 3b, Extended Data Fig. 5b)**. Reduction in the rate of internalization of CD44 but not TfR1 was also observed in ether lipid-deficient PyMT-1099 TGF-β-treated cells **(Fig. 3c, 3d, Extended Data Fig. 5c, 5d)**. Therefore, ether lipids play a critical role in modulating intracellular iron levels by regulating endocytosis of CD44 but not transferrin receptor. These findings were consistent with our previous observations that TfR1 and CD44 localize to distinct endocytic vesicles in CSC-enriched cancer cells[35, 48], making plausible that their internalization was governed by distinct endocytic mechanisms.

To further support the role of CD44 in promoting iron uptake—acting via endocytosis of HA—we demonstrate that knocking out the gene encoding CD44 or, alternatively, treating cancer cells with the HA-degrading enzyme, hyaluronidase, led to a reduction in intracellular iron levels **(Fig. 3e)**. Conversely, supplementing WT cells with HA significantly increased intracellular iron levels **(Fig. 3e)**. Similar observations were seen in human OVCAR8 cells **(Extended Data Fig. 7f)**. Taken together, these observations further supported the central role of CD44 in mediating iron uptake in these cancer cells[35].

We then studied whether the defect in CD44 endocytosis observed in ether lipid-deficient cells was limited specifically to CD44 or other cell-surface proteins internalized

by a similar mechanism. CD44 is known to undergo a type of clathrin- and dynamin-independent form of endocytosis[48-50]. To test whether loss of ether phospholipids had a wider effect on the clathrin- and dynamin-independent mode of endocytosis, we examined the rate of uptake of dextran (70 kDa), a branched polysaccharide known to undergo endocytosis by a clathrin-independent mechanism[49] (pinocytosis). Similar to CD44, we observed that loss of AGPS also induced a significant reduction in the rate of dextran endocytosis; this behavior could be reversed by restoration of ether phospholipid levels achieved by AGPS addback **(Fig. 3f, 3g, Extended Data Fig. 5e, 5f).**

The internalization mechanism of CD44 and dextran differs from that of many plasma-membrane proteins, including TfR1 and EGFR, which undergo clathrin-dependent endocytosis, in which small invaginations of clathrin-coated pits undergo scission facilitated by the GTPase dynamin[49, 51]. As predicted by the distinct actions of these two mechanisms, we observed that loss of ether lipids had a negligible effect on the rate of EGFR endocytosis **(Fig. 3h, Extended Data Fig. 6a, 7a-b).** Taken together, these observations indicate that internalization of extracellular and cell-surface molecules is mediated by distinct mechanisms which differ in their dependence on plasma membrane ether phospholipids.

To further characterize the clathrin-independent mechanism used by CD44 and dextran, we next pursued both genetic and pharmacologic approaches that target against either the CLIC/GEEC pathway or pinocytosis. We found that inhibition of the CLIC/GEEC pathway via siRNA-mediated knockdown of PICK1[52] or treatment with 7-keto-cholesterol[53, 54] significantly reduced CD44 internalization, which in turn led to decreased total cellular and lysosomal iron **(Extended Data Fig. 8a-8c, 8e, 8g, 8h)**. We also show that blocking pinocytosis via knockdown of CtBP1[55-57] or treatment with Cytochalasin-D[58] is capable of impairing CD44 internalization (albeit, to a lesser extent than CLIC/GEEC inhibition), resulting in lower but non-significant reductions in total cellular and lysosomal iron **(Extended Data Fig. 8a-8c, 8d, 8f, 8h)**. These findings suggest that CD44 internalization depends more on the CLIC/GEEC pathway than on pinocytosis for iron delivery into cells.

Given that polyunsaturated phospholipids have been shown to promote endocytosis[59], we investigated whether treatment with exogenous polyunsaturated fatty acids (PUFAs) could compensate for loss of ether lipids in regulating CD44 endocytosis. We observed that supplementation with exogenous PUFAs could not fully rescue impaired CD44 endocytosis induced by loss of ether lipids **(Fig. 3i, Extended Data Fig. 6b)**. Furthermore, while liposomes containing ester-linked PUFA-PE phospholipids could only partially rescue CD44 endocytosis, ether-linked PUFA-PE or -PC liposomes achieved an even greater degree of rescue, with ether-linked PUFA-PE liposomes fully restoring CD44 endocytosis to levels exceeding those of WT cells **(Fig. 3j, Extended Data Fig. 6c)**. These findings demonstrate that both the presence of the ether linkage in phospholipids as well as the type of headgroup present within phospholipids play important roles in supporting efficient CD44-mediated endocytosis.

Ether lipid deficiency impairs membrane biophysical properties

The above observations did not provide mechanistic insights into how changes in the composition of membrane ether lipids could exert an effect on CD44 internalization.

As observed by others, non-clathrin-mediated endocytosis, which is employed by CD44, is particularly sensitive to changes in the physicochemical properties of the lipid bilayer forming plasma membranes[50, 60-65]. Such changes can influence membrane tension and fluidity and the stability and formation of lipid rafts, all of which impact the assembly and dynamics of clathrin-independent, cell-surface endocytic structures. Hence, we hypothesized that ether lipids alter the biophysical properties of the plasma membrane to facilitate elevated iron endocytosis via CD44. To substantiate these hypotheses, we quantified the abundance of ether lipids in the plasma membrane. Lipidomics profiling of pB3-derived giant plasma membrane vesicles (GPMV) showed that ether lipids make up ~23% of plasma membrane lipids and are depleted to ~5% upon AGPS KO **(Extended Data Fig. 9a-f)**.

Alterations in membrane tension have long been demonstrated to affect endocytosis[66-71]. This prompted us to assess the effects of ether lipid deficiency on plasma membrane tension. Membrane tension measures the forces exerted on a defined cross-section of the plasma membrane, which is influenced by both the in-plane tension of the lipid bilayer and the attachment of the plasma membrane to the underlying cell cortex[72, 73].

To quantify membrane tension directly, we generated a membrane tether using an optically trapped bead and measured the pulling force (f) and the tube radius (R) to calculate membrane tension (σ) of living cells[59, 74] **(Fig. 4a, 4b).** We found that depletion of ether phospholipids led to a significant increase in membrane tension in pB3 AGPS KO cells relative to the corresponding pB3 WT cells **(Fig. 4c)**. This shift was largely attenuated upon restoration of AGPS expression in pB3 AGPS KO cells or upon exposure of cultured cells to liposomes composed of ether phospholipids **(Fig. 4c)**. Consistent with earlier measurements, treatment of pB3 AGPS KO cells with ether PUFA-PE liposomes increased the rate of CD44 endocytosis to levels comparable to those of pB3 WT cells**.** In contrast, treatment of pB3 AGPS KO cells with liposomes derived from monounsaturated phosphatidylethanolamine (MUFA-PE) ether lipids only partially rescued CD44 endocytosis **(Fig. 4d, Extended Data Fig. 6d)**. No changes were observed in the rate of clathrin-dependent TfR1 endocytosis under these conditions **(Fig. 4e, Extended Data Fig. 6e)** and loss of CD44 showed modest effects on membrane tension **(Extended Data Fig. 7d-7e)**. Taken together, these results provide evidence that ether lipids facilitate CD44-mediated iron endocytosis in cancer cells, in part by decreasing membrane tension.

Membrane lipid packing can also impact endocytosis[75-77]. This is related to the fluidity or viscosity of the lipid bilayer, with higher lipid packing correlating with higher viscosity. This affects the ease with which proteins and lipids undergo lateral diffusion and conformational changes within a lipid bilayer, thereby affecting endocytosis-related signaling[59]. This prompted us to investigate the contribution of ether lipids to membrane lipid packing. We used C-laurdan, a lipid-based, polarity-sensitive dye, which yields a spectral emission shift dependent on the degree of lipid packing[78]. These measurements are used to calculate a unitless index, termed generalized polarization (GP), where a higher GP indicates increased lipid packing[78]. Our measurements using C-laurdan indicated that a reduction in ether lipid levels resulted in a measurable and significant increase in membrane packing **(Fig. 4f-4h)** which, like increases in membrane tension, negatively affects membrane deformability[75].

The association of CD44 with lipid rafts, which are dynamic plasma membrane nanodomains, is known to be critical for CD44-mediated HA endocytosis[79]. We reasoned that a decrease in the stability of lipid rafts, would result in impairment of CD44 endocytosis[80]. Accordingly, we measured the miscibility transition temperature (T_{misc}) which is hypothesized to be related to the stability membrane domains of isolated cellular plasma membranes. We observed a decrease in T_{misc} upon loss of AGPS in pB3 cells, which indicate a decrease in lipid raft stability **(Fig. 4i, Extended Data Fig. 7c)**. This finding supports a role for ether lipids in maintaining the plasma membrane organization through lipid raft microdomains, revealing yet another biophysical property of lipid bilayers that can influence CD44 endocytosis.

It is noteworthy that clathrin-independent endocytosis exhibits a greater dependency on the membrane biophysical properties assessed above[50, 60-65]. This may explain why loss of ether lipids can exert a significant effect on the rate of clathrin-independent, CD44-mediated iron endocytosis but negligible effects on the clathrin-dependent TfR1 endocytosis. Furthermore, these findings revealed a mechanism by which membrane-associated ether lipids could govern a major mechanism of iron internalization, which may impact the vulnerability of cancer cells to ferroptosis inducers.

Loss of ether lipids decreases metastasis and cancer cell stemness

Prior studies have demonstrated that reduced membrane tension and elevated intracellular iron can promote cancer metastasis[81-85]. These findings prompted us to investigate whether changes in the ether lipid composition of cancer cells impact key steps of the multi-step invasion-metastasis cascade, notably extravasation efficiency, post-extravasation proliferation[86] and importantly stemness as manifested by tumor-initiating ability.

We measured extravasation efficiency by employing an in vitro three-dimensional microvascular network system composed of human umbilical vein endothelial cells (HUVECs) and normal human lung fibroblasts. This system has been shown to accurately model some of the complex biological processes associated with cancer cell extravasation[87-91]. Using this defined experimental system, we found that loss of ether lipids significantly decreased extravasation efficiency **(Fig. 5a-5c)**. Furthermore, we observed a strong reduction in overall metastatic burden following intracardiac injection in syngeneic hosts of the pB3 AGPS KO cells relative to corresponding WT cells **(Fig. 5d-5f)**. We note that ether lipid deficiency had a modest effect on primary tumor growth kinetics **(Fig. 5g-5i)**. A decrease in metastatic burden was also observed upon knockout or *AGPS* and *FAR1* in OVCAR8 cells, and upon loss of CD44 in pB3 cells **(Extended Data Fig. 10a-10c)**.

Given that high CD44 expression and elevated intracellular iron levels are positively correlated with cancer cell stemness[35, 44, 92], we investigated whether ether lipid deficiency could modulate CSC properties, by employing mammosphere formation assays[93] and experimental limiting dilution tumor-implantation studies. These experiments indicated that loss of ether lipids in pB3 cells decreases cancer cell stemness **(Fig. 5j, Extended Data Fig. 10d-10e)**, which, as we have found in other investigations, serve as a reliable marker of metastasis-initiating capacity[94].

Additionally, we show that treatment of human MCF7 breast adenocarcinoma cells with oncostatin M (OSM) increases the sub-population $CD44^{hi}/CD24^{lo}$ cells

(Extended Data Fig. 11a, 11b), resulting in elevated PUFA-containing ether phospholipids and increased intracellular iron **(Extended Data Fig. 11c-11g).** This is consistent with our TGFβ-treated PyMT-1099 model **(Extended Data Fig. 12a-12c)**.

Moreover, we found that loss of ether lipids significantly attenuates the tumor-initiating potential and metastatic capacity of PyMT-1099 AGPS KO TGF-β-treated cells following orthotopic implantation into the mammary stromal fat pad compared to PyMT-1099 WT TGF-β-treated cells **(Fig. 5k-5m)**. Collectively, our findings indicate that ether lipids play critical roles in promoting cancer cell stemness and resulting post-extravasation colonization.

DISCUSSION

Our findings underscore the importance of integrating membrane biophysical properties into existing genetic and biochemical frameworks for understanding cancer cell fate. While phospholipids have long been implicated in cellular transformation, the focus thus far has primarily been to study the actions of specific lipids (e.g. inositol phospholipids) and their signaling derivatives[95]. Our study reveals a distinct and underappreciated mechanism by which lipids influence malignancy. Specifically, we identify ether lipids as key modulators of plasma membrane biophysical properties that regulate iron uptake and neoplasia-related phenotypes such as metastasis and cancer cell stemness/tumor-initiating potential. Importantly, this biophysical configuration creates a unique vulnerability of cancer cells to ferroptosis and suggests that targeting lipid metabolism and iron homeostasis could be exploited to suppress subpopulations of highly metastatic and drug-tolerant carcinoma cells[7, 96].

Ether phospholipids have been widely characterized as participants in ferroptosis through their role as substrates prone to iron-catalyzed oxidation[22]. However, our findings indicate an entirely distinct biochemical mechanism is operative here, whereby ether lipids directly modulate the levels of intracellular iron, a rate-limiting parameter governing ferroptosis susceptibility[4, 35, 82]. By emphasizing the role of membrane biophysical properties in mediating iron uptake, we depart from the conventional portrayal of phospholipids simply as substrates of oxidation. This shift in perspective has the potential to open new avenues for research, as it challenges researchers to explore the biophysical aspects of membranes as a new dimension in the regulation of this cell death program.

Although most lipid classes remained largely unchanged upon AGPS KO, it is plausible that subtle changes in membrane lipid composition beyond ether lipid levels may also be responsible for the phenotypes described here. Moreover, in addition to perturbed membrane receptor dynamics promoted by changes in membrane tension, the observed decrease in metastatic capacity of AGPS KO cells may also result from changes in oncogenic signaling lipids[24], mechanisms that are not addressed here.

Alterations in intracellular iron level can impact gene expression via various mechanisms, including modulation of chromatin-modifying enzyme activity[35, 97, 98]. For example, an increase of intracellular iron levels has been shown to promote the activity of iron-dependent histone demethylases[35, 97, 98], impacting gene expression profiles underlying cell plasticity[35] and immune cell activation[39]. Our finding that ether lipid deficiency reduces intracellular iron levels explains, at least in part, how loss of ether

lipids may affect cancer-associated transcriptional programs, acting at the epigenetic level and enabling a variety of malignancy-associated cell phenotypes including metastasis and cancer stemness. Such mechanisms may act in concert with processes independent from iron, which are also regulated by ether lipids to affect cancer malignancy traits.

In the longer term, the implications of our findings may reach well beyond cancer pathogenesis. Thus, we suggest that the interplay between membrane biophysics and iron biology could represent a fundamental determinant of cell fate, influencing diverse processes such as differentiation, immune activation, wound healing, and embryonic development.

ACKNOWLEDGMENTS

We thank all members of the Weinberg, Farese and Walther labs for insightful discussions and reagents. We are grateful to Brent Stockwell, Laurie Boyer, Edward Lyman, and Fred Heberle for helpful discussions. We acknowledge technical support from Caroline A. Lewis, Zon W. Lai and Marina Plays, the CurieCoreTech Metabolomics and Lipidomics Technology Platform at the Institut Curie, the following facilities at the Whitehead Institute: Metabolite Profiling Core, W.M. Keck Microscopy Core, Flow Cytometry Core, as well as the Koch Institute's Robert A. Swanson (1969) Biotechnology Center, specifically the MIT Koch Institute Animal Imaging and Pre-Clinical Testing Core Facility and Hope Babette Tang (1983) Histology Core Facility. We also thank Naviya Kapadia for assistance with proofreading and providing helpful comments on the manuscript and figures.

This work was funded in part by the National Institutes of Health: Koch Institute Support (core) Grant P30CA014051 from the National Cancer Institute (WSH), National Institute Of General Medical Sciences R37GM058615 (VWH), the National Cancer Institute K99CA255844/R00CA255844 (NB), and the National Cancer Institute (RDK). Additional funding support was received from MIT Stem Cell (RAW), Brendan Bradley Gift (RAW), Nile Albright Research Foundation (RAW), Samuel Waxman Cancer Research Foundation (RAW), Virginia and D.K. Ludwig Fund for Cancer Research Center (RAW), Marble Center for Cancer Nanomedicine (PTH), Jane Coffin Childs Memorial Fund (WSH), Ludwig Center at MIT's Koch Institute for Integrative Cancer Research (WSH), Emerald Foundation, Inc. (WSH), National Institute Of General Medical Sciences 1R21CA300756 (KRL), National Institute Of General Medical Sciences R35GM134949 (IL), National Institute Of General Medical Sciences T32GM136540 (RPM & JS) and the New Horizon UROP Fund/MIT (VVP). R.R. is supported by Ligue Contre le Cancer (Equipe Labellisée), Fondation Charles Defforey-Institut de France, Fondation Bettencourt Schueller, Institut National du Cancer, Agence Nationale de la Recherche and the European Research Council under the European Union's Horizon 2020 research and innovation program (grant agreement no. 647973). R.R. also received support from INCa 2022-1-PL BIO-05-ICR-1 and INCa_16712.

AUTHOR CONTRIBUTIONS

W.S.H. and R.R. conceived the project. W.S.H, R.P.M. and S.M. designed and performed experiments with input from R.A.W. and R.R. S.M. conducted iron measurement studies. S.M. and J.L.S. performed oxidized lipidomics analysis. J.Y. perfomed endocytosis assays, with critical insight from V.W.H. Membrane tension studies were conducted by S.I., with support from A.E.C. on data analysis. K.R.L. performed membrane tension experiments and together with I.L. provided key insights on interpretation. W.S.H., S.D. and F.R. conducted animal experiments. Z.W. performed extravasation assays. A.D. and C.B.C provided significant evaluation and interpretation of lipidomics data. Liposomal nanoparticles and HA-Cy3 probes were synthesized by N.B. and A.V. All other authors contributed to data acquisition and analysis. W.S.H., and R.P.M. wrote the manuscript. W.S.H., R.A.W., and R.R. edited the manuscript with input from all authors.

COMPETING INTERESTS

The authors declare no competing interests.

METHODS

Cell lines

The pB3 MMTV-PyMT-derived murine breast cancer cell line was a kind gift from the laboratory of Harold L. Moses[32]. 687g cells (also called EpCAM^{Lo}Snail-YFP^{Hi}) were originally established from tumors that developed in the MMTV-PyMT-Snail-IRES-YFP reporter mouse model, previously developed by the Weinberg lab[99]. pB3 and 687g cell lines were cultured in 1:1 DMEM/F12 medium containing 5% adult bovine serum with 1% penicillin-streptomycin and 1% non-essential amino acids[32]. The PyMT-1099 murine breast cancer cell line was a kind gift from the laboratory of Gerhard Christofori and cultured in DMEM supplemented with 10% fetal bovine serum, 1% penicillin-streptomycin and 1% glutamine[29]. For select experiments, these cells were treated with 2 ng/ml of TGF-β for 10 days prior to performing subsequent analyses. OVCAR8 cells were obtained from the laboratory of Joan Brugge and cultured in 1:1 MCDB 105 medium/Medium 199 Earle's Eagles medium supplemented with 10% fetal bovine serum and 1% penicillin-streptomycin. MCF7 (ATCC, HTB-22) cells were cultured in Dulbecco's Modified Eagle Medium GlutaMAX (DMEM, ThermoFisher Scientific, 61965059) supplemented with 10% Fetal Bovine Serum and Penicillin-Streptomycin mixture (BioWhittaker/Lonza, DE17-602E) and treated with oncostatin M (OSM, R&D systems, 295-OM-050, 100 ng/mL, 72 h). All cells were cultured in a humidified incubator at 37°C with 5% CO_2. All cells were negative for mycoplasma. Human cell line authentication (CLA) analysis of OVCAR8 cells were performed by the Duke University DNA Analysis facility. Established murine lines have not been STR profiled.

Animal studies

All animal studies received ethical approval and were conducted according to the MIT Committee on Animal Care protocol. For primary tumor growth studies: 1 million cells were resuspended in 20% Matrigel/PBS and injected into the mammary fat pad of 6-8

weeks old female mice. C57BL/6 mice (Jackson Laboratories) were used for in vivo experiments with pB3 cells. NSG mice were used for in vivo experiments with PyMT-1099 cells. These cells were pretreated with TGF-β (2 ng/ml) for 10 days prior to injection. Tumor size was measured once a week using a vernier caliper and tumor volume was calculated using the formula: Tumor volume = (length x width^2)/2, where length represents the largest tumor diameter, and width represents the perpendicular tumor diameter. For limiting dilution tumor-initiating assays, pB3 WT or pB3 AGPS KO cells were resuspended in 20% Matrigel/PBS and injected into the mammary fat pad of 6-8 weeks old female C57BL/6 mice (Jackson Laboratories) at the following dilutions: 100,000, 10,000, 1000, 100 cells. Animals were assessed for palpable tumors after 39 days post injection. The estimated number of CSCs was calculated using the extreme limiting dilution analysis (ELDA) software[100]. For experimental metastasis involving pB3 cell lines, 0.2 million cells were resuspended in 200µl of PBS and injected into the left ventricle of 6-8 weeks old female C57BL/6 mice. Metastatic burden was measured after 10 d post-injection via bioluminescence in live animals using the spectrum in vivo imaging system (IVIS)[101]. Images were analyzed using Living Image software (PerkinElmer, version 4.8.2). For OVCAR8 cells, 1.5 million cells were resuspended in PBS and implanted into 6-8 weeks old female athymic nude mice (Jackson Laboratories) via intraperitoneal injections. Metastatic burden was assessed after 6 weeks using a fluorescence dissecting microscope.

Generation of gene-edited cell lines using CRISPR/Cas9

Except for OVCAR8 cells, all AGPS KO single-cell clones were generated via transient transfection with mouse AGPS CRISPR/Cas9 KO Plasmids (Catalog no. sc-432759, Santa Cruz) according to the manufacturer's instructions. GFP-positive cells were sorted via fluorescence-activated cell sorting (FACS) into 96-well plates with one cell per well and single-cell clones were subsequently expanded. AGPS KO single-cell clones were assessed for loss of AGPS expression via western blot analysis. pB3 and PyMT-1099 AGPS addback cells were generated by transducing an AGPS KO single-cell clone with pLV[Exp]-Puro-EF1A-mAgps lentiviral vector (VectorBuilder). pB3 and PyMT-1099 AGPS KO cells expressing pLV[Exp]-Puro-EF1A-Stuffer_300bp (VectorBuilder) were established as controls for AGPS addback experiments and noted in the figure legends where used. Lentivirus was produced by transfecting HEK293T cells with viral envelope (VSVG, Addgene) and packaging plasmids (psPAX2, Addgene). Viral supernatant was collected after 48 h and filtered through a 0.45µm filter. Stably transduced cells were selected with 2 µg/ml puromycin. OVCAR8 FAR1 KO and AGPS KO single cell clones as well as nontargeting control cells were established as previously described[22]. pB3 CD44 KO cells (bulk) were generated using human CD44 CRISPR/Cas9 KO Plasmids (Catalog no. sc-419558, Santa Cruz) according to the manufacturer's instructions. After 48 h post-transfection, cells were sorted by flow cytometry for GFP positive cells, expanded in culture, and re-sorted twice for CD44 negative cells using Alexa Fluor® 647 anti-mouse/human CD44 Antibody. Cells were maintained as bulk CD44 KO cells.

Plasmid information

The table below indicates the plasmids used to generate gene-edited cell lines.

Plasmid	**Source**
pLV[Exp]-Puro-EF1A-Agps (mouse)	VectorBuilder
pLV[Exp]-Puro-EF1A-Stuffer_300bp	VectorBuilder
Mouse AGPS CRISPR/Cas9 KO Plasmids	Catalog no. sc-432759, Santa Cruz
Mouse CD44/HCAM CRISPR/Cas9 KO Plasmids	Catalog no. sc-419558, Santa Cruz
LentiCRISPRv2-puro-Nontargeting	Published[22]
LentiCRISPRv2-puro-human AGPS sg	Published[22]
LentiCRISPRv2-puro-human FAR1 sg	Published[22]
pLV-EF1A-eGFP-LUC	VectorBuilder
pCDH-EF1-Luc2-P2A-tdTomato	Plasmid #72486, Addgene

Lipidomics analysis

Sample preparation (whole cell preparations)
Briefly, $1x10^6$ cells were plated in individual wells of a 6 well dish. No more than 16 hours later, cells were washed with DPBS (Dulbecco's PBS without Mg and Ca), trypsinized, and washed twice again with before resuspending in 300uL of DPBS and storing at -80°C until further processing.

Sample preparation (GPMV preparations)
Giant plasma membrane vesicles (GPMVs) were isolated from pB3 WT, AGPS KO, and AGPS addback, as previously described with minor modifications[102]. Briefly, three 10-cm dishes of approximately 70% confluency prepared for each cell line were washed once with phosphate-buffered saline (PBS) and twice with GPMV buffer (10mM HEPES, 150mM NaCl, 2mm CaCl2 – pH 7.4). Fresh N-ethylmaleimide (Millipore Cat. No. E3876-5G) was added to GPMV buffer to yield a final concentration of 5 mM, then 4mL of this buffer was added to each culture dish followed by incubation for 3 hours at 37°C. Supernatants containing GPMVs were then collected and pooled for each condition and passed through 5 µm centrifugal filters (Millipore Sigma Cat. No. UFC30SV00) by centrifuging at 500rcf to remove any whole cells. The pooled filtrates were subsequently centrifuged at 20,000 × g for 2 hours at 4°C and resuspended in 300 µL of DPBS. The presence of vesicles was confirmed by light microscopy before storing at -80°C until further processing. Three independent biological replicates were collected and used for lipidomic analysis.

Lipid extraction for mass spectrometry lipidomics
Mass spectrometry-based lipid analysis was performed by Lipotype GmbH (Dresden, Germany) as described[103]. Lipids from whole cells or isolated GPMVs were extracted

using a chloroform/methanol procedure[104]. Samples were spiked with internal lipid standard mixture containing: cardiolipin 14:0/14:0/14:0/14:0 (CL), ceramide 18:1;2/17:0 (Cer), diacylglycerol 17:0/17:0 (DAG), hexosylceramide 18:1;2/12:0 (HexCer), lyso-phosphatidate 17:0 (LPA), lyso-phosphatidylcholine 12:0 (LPC), lyso-phosphatidylethanolamine 17:1 (LPE), lyso-phosphatidylglycerol 17:1 (LPG), lyso-phosphatidylinositol 17:1 (LPI), lyso-phosphatidylserine 17:1 (LPS), phosphatidate 17:0/17:0 (PA), phosphatidylcholine 17:0/17:0 (PC), phosphatidylethanolamine 17:0/17:0 (PE), phosphatidylglycerol 17:0/17:0 (PG), phosphatidylinositol 16:0/16:0 (PI), phosphatidylserine 17:0/17:0 (PS), cholesterol ester 20:0 (CE), sphingomyelin 18:1;2/12:0;0 (SM), triacylglycerol 17:0/17:0/17:0 (TAG). After extraction, the organic phase was transferred to an infusion plate and dried in a speed vacuum concentrator. The dry extract was re-suspended in 7.5 mM ammonium formate in chloroform/methanol/propanol (1:2:4, V:V:V). All liquid handling steps were performed using Hamilton Robotics STARlet robotic platform with the Anti Droplet Control feature for organic solvents pipetting.

MS data acquisition

Samples were analyzed by direct infusion on a QExactive mass spectrometer (Thermo Scientific) equipped with a TriVersa NanoMate ion source (Advion Biosciences). Samples were analyzed in both positive and negative ion modes with a resolution of $R_{m/z=200}$=280000 for MS and $R_{m/z=200}$=17500 for MSMS experiments, in a single acquisition. MSMS was triggered by an inclusion list encompassing corresponding MS mass ranges scanned in 1 Da increments[105]. Both MS and MSMS data were combined to monitor CE, DAG and TAG ions as ammonium adducts; LPC, LPC O-, PC, PC O-, as formate adducts; and CL, LPS, PA, PE, PE O-, PG, PI and PS as deprotonated anions. MS only was used to monitor LPA, LPE, LPE O-, LPG and LPI as deprotonated anions; Cer, HexCer and SM as formate adducts.

Data analysis and post-processing

Data were analyzed with in-house developed lipid identification software based on LipidXplorer[106, 107]. Only lipid identifications with a signal-to-noise ratio >5, and a signal intensity 5-fold higher than in corresponding blank samples were considered for further data analysis. Cholesterol was removed from each data set before analysis. Simple imputation was performed by replacing missing values with 0.2 * the minimum non-zero value for each lipid assayed, a modification from previously described methods[108]. Relative mol% levels of individual lipid species were determined by dividing each pmol value by the sum pmol of all lipids detected in that sample and multiplying by 100. Total ether lipid (and other lipid classes presented) were calculated by summation of mol% values of each lipid within that class. Lipid fold changes were calculated by dividing the average mol% of each lipid species between groups and applying a Log2 transformation. Corresponding p-values were calculated using the students t-test.

Oxidized lipidomics

Sample preparation

100,000 cells per condition were plated in 6-well plates 24 h prior to the experiment. For PyMT-1099, cells were treated with TGF-β (2 ng/mL) for 10 d. pB3 cells were treated with 500 nM RSL3, OVCAR8 cells with 2 µM ML210 and TGF-β-treated PyMT-1099 cells with 10 µM ML210 for 24 h. Cells were subsequently washed with PBS and then with 150 mM ammonium bicarbonate. Cells were then scraped and resuspended in 150 mM ammonium bicarbonate and centrifuged at 300 g for 5 min. The supernatant was removed, and cells were resuspended in 1 mL of 150 mM ammonium bicarbonate. The solutions were centrifuged at 12,000 RPM for 10 min and the supernatant was removed. 200 µL of 150 mM sodium bicarbonate was added to the pellet and samples were flash frozen in liquid nitrogen. Cells were prepared in 5 independent biological replicates and lipidomics analysis was performed on the same day for all the replicates.

Lipid extraction for mass spectrometry lipidomics

For lipidomics analysis, the 200 µL cell lysates were spiked with 1.4 µL of internal standard lipid mixture containing 300 pmol of phosphatidylcholine 17:0-17:0, 50 pmol of phosphatidylethanolamine 17:0-17:0, 30 pmol of phosphatidylinositol 16:0-16:0, 50 pmol of phosphatidylserine 17:0-17:0, 30 pmol of phosphatidylglycerol 17:0-17:0 and 30 pmol of phosphatidic acid 17:0-17:0 and subjected to lipid extraction at 4 °C, as previously described[109]. The sample was then extracted with 1 mL of chloroform-methanol (10:1) for 2 h. The lower organic phase was collected, and the aqueous phase was re-extracted with 1 mL of chloroform-methanol (2:1) for 1 h. The lower organic phase was collected and evaporated in a SpeedVac vacuum concentrator. Lipid extracts were dissolved in 100 µL of infusion mixture consisting of 7.5 mM ammonium acetate dissolved in propanol:chloroform:methanol [4:1:2 (vol/vol)].

MS data acquisition

Samples were analyzed by direct infusion in a QExactive mass spectrometer (Thermo Fisher Scientific) equipped with a TriVersa NanoMate ion source (Advion Biosciences). 5 µL of sample were infused with gas pressure and voltage set to 1.25 psi and 0.95 kV, respectively. PC, PE, PEO, PCOx and PEOx were detected in the 10:1 extract, by positive ion mode FTMS as protonated adducts by scanning m/z= 580–1000 Da, at $R_{m/z=200}$=280 000 with lock mass activated at a common background (m/z=680.48022) for 30 s. Every scan is the average of 2 micro-scans, automatic gain control (AGC) was set to 1E6 and maximum ion injection time (IT) was set to 50 ms. PG and PGOx were detected as deprotonated adducts in the 10:1 extract, by negative ion mode FTMS by scanning m/z= 420–1050 Da, at $R_{m/z=200}$=280 000 with lock mass activated at a common background (m/z=529.46262) for 30 s. Every scan is the average of 2 micro-scans. Automatic gain control (AGC) was set to 1E6 and maximum ion injection time (IT) was set to 50ms. PA, PAOx, PI, PIOx, PS and PSOx were detected in the 2:1 extract, by negative ion mode FTMS as deprotonated ions by scanning m/z= 400–1100 Da, at $R_{m/z=200}$=280 000 with lock mass activated at a common background (m/z=529.46262) for 30 s. Every scan is the average of 2 micro-scans, automatic gain control (AGC) was set to 1E6 and maximum ion IT was set to 50 ms. All data was acquired in centroid mode. All lipidomics data were analyzed with the lipid identification software, LipidXplorer[107]. Tolerance for MS and identification was set to 2 ppm. Data were normalized to internal standards.

Immunoblotting
Cells were washed with ice-cold PBS and lysed in cell lysis buffer (Cell Signaling Technology, Cat. #9803S) containing 1mM PMSF protease inhibitor (Cell Signaling Technology, Cat. #8553S). Protein samples were prepared with NuPAGE LDS Sample Buffer (Thermo Fischer Scientific, Cat. #NP0007), NuPage Sample Reducing Agent (Thermo Fischer Scientific, Cat. #NP0004) or 2X Laemmli buffer and heated at 70 ºC or 94 ºC for 10 minutes. Samples were resolved by SDS-PAGE, transferred to nitrocellulose (Bio-Rad) and blocked in 5% milk/TBST or 5% milk/PBST for 1 h at room temperature. Membranes were incubated overnight with the respective primary antibodies at 4 ºC in 5% milk/PBST or in 5% BSA/TBST, washed with TBST or PBST, incubated with HRP-conjugated secondary antibodies and developed using SuperSignal™ West Dura, the SuperSignal™ West Pico PLUS, or the SuperSignal™ West Femto kits (ThermoFisher Scientific, Cat. 34076, Cat. 34580 and Cat. 34096).

Antibody information
The table below indicates the antibodies used for western blotting and flow cytometry analyses.

Antibody	**Source**	**Catalog No.**
E-Cadherin (CDH1)	Cell Signaling Technology	3195S
Fibronectin (FN1)	Abcam	ab45688
γ-Tubulin	Sigma-Aldrich	T5326
MGLL	Abcam	ab24701
CtBP1	Alberto Luini (Institute of Biochemistry and Cell Biology, National Research Council, Italy).	-
PICK1	Cell Signaling Technology	85325S
Zeb1	Cell Signaling Technology	3396S
N-cadherin	Cell Signaling Technology	13116S
AGPS	Invitrogen	PA5-56400
FAR1	Novus Bio.	NBP1-89847
Snail	Cell Signaling Technology	3879S
Vimentin	Cell Signaling Technology	5741S

GAPDH	Cell Signaling Technology	2118S
CD44 (Western Blot)	Abcam	ab189524
Anti-rabbit IgG, HRP-linked antibody	Cell Signaling Technology	7074S
Anti-mouse IgG, HRP-linked antibody	Cell Signaling Technology	7076S
SMAD2/3	Cell Signaling Technology	3102S
Phospho-SMAD2 (Ser465/467)/SMAD3 (Ser423/425)	Cell Signaling Technology	8828S
Brilliant Violet 605™ anti-human CD24 Antibody	BioLegend	311124311124
CD44 Antibody (MEM-263) [Alexa Fluor® 647]	Novus Biologicals	NB500-481AF647
Alexa Fluor® 647 anti-mouse/human CD44 Antibody	BioLegend	103017

Cell viability assay
Cells were seeded in 96-well black clear bottom plates (Corning) at 2000 or 3000 cells (PyMT-1099 +/- TGF-β) and 6000 cells (OVCAR8) per well. Approximately, 12-16 h post-seeding, cells were treated with various drug concentrations using an HP D300e Digital Dispenser unless stated otherwise. Cell viability was assessed at 72 h post-treatment by performing CellTiter-Glo Luminescent Cell Viability Assays (Promega) according to the manufacturer's instructions. Relative viability was calculated by normalizing to untreated controls unless stated otherwise. Non-linear regression models (four parameter, variable slope) were applied to generate the regression fit curves using GraphPad Prism version 10.4.1. Drug compounds were purchased as indicated: RSL3 (Selleck Chem), ML210 (Sigma Aldrich), and Liproxstatin-1 (Fisher Scientific). For experiments involving ferric ammonium citrate (FAC), FAC (Sigma) was prepared fresh in sterile 1× PBS and manually added directly to cell culture media at the indicated concentrations at the time of seeding into 96-well plates. Unless stated otherwise, cells were pretreated with FAC for 24 h prior to ML210 treatment.

Inductively coupled plasma mass spectrometry (ICP-MS)
For select experiments, cells were treated for 24 h with hyaluronic acid (Carbosynth, FH45321, 600-1000 kDa, 1 mg/mL) or hyaluronidase (HD, Sigma-Aldrich, H3884, 0.1

mg/mL) as indicated. Glass vials equipped with Teflon septa were cleaned with nitric acid 65% (VWR, Suprapur, 1.00441.0250), washed with ultrapure water (Sigma-Aldrich, 1012620500) and dried. Cells were harvested and washed twice with 1× PBS. Cells were then counted using an automated cell counter (Entek) and transferred in 200µL 1× PBS to the cleaned glass vials. The same volume of PBS was transferred into separate vials for the background subtraction, at least in duplicate per experiment. For tumor samples, small pieces of the tumors were added into pre-weighed cleaned glass vials. Samples were lyophilized using a freeze dryer (CHRIST, 22080). Glass vials with lyophilized tumor samples were weighed to determine the dry weight for normalization. Samples were subsequently mixed with nitric acid 65% and heated at 80°C overnight. Samples were diluted with ultrapure water to a final concentration of 0.475 N nitric acid and transferred to metal-free centrifuge vials (VWR, 89049-172) for subsequent ICP-MS analyses. Amounts of metals were measured using an Agilent 7900 ICP-QMS in low-resolution mode, taking natural isotope distribution into account. Sample introduction was achieved with a micro-nebulizer (MicroMist, 0.2 mL/min) through a Scott spray chamber. Isotopes were measured using a collision-reaction interface with helium gas (5 mL/min) to remove polyatomic interferences. Scandium and indium internal standards were injected after inline mixing with the samples to control the absence of signal drift and matrix effects. A mix of certified standards was measured at concentrations spanning those of the samples to convert count measurements to concentrations in the solution. Values were normalized against cell number or dry weight.

Iron measurements using HRhoNox-M

The lysosome-specific fluorescent Fe(II) probe HRhoNox-M was synthesized in 3 steps according to a previously published procedure[36]. ^{1}H NMR (300 MHz, $CDCl_3$) δ 7.93 (1H, d, *J* = 2.0 Hz), 7.45 (1H, dd, *J* = 8.5 Hz, 2.0 Hz), 7.40–7.30 (3H, m), 7.05 (1H, d, *J* = 8.5 Hz), 6.90 (1H, d, *J* = 7.0 Hz), 6.80 (1H, d, *J* = 8.0 Hz), 6.50–6.44 (2H, m), 5.28–5.35 (2H, m), 3.62 (6H, m), 2.97 (6H, s). MS (ESI) m/z: calcd. for $C_{24}H_{25}N_2O_3$ $[M+H]^+$ 389.19, found: 389.35. Cells were incubated with 1 µM HRhoNox-M for 1 h or lysotracker deep red (Thermo Fisher Scientific L12492) according to the manufacturer's instructions for 1 h. Cells were then washed twice with ice-cold PBS and suspended in incubation buffer prior to being analyzed by flow cytometry. For each condition, at least 10,000 cells were counted. Data were recorded on a BD Accuri C6 (BD Biosciences) and processed using Cell Quest (BD Biosciences) and FlowJo (FLOWJO, LLC). The signal for HRhoNox-M was normalized against the signal of lysotracker of cells treated in parallel.

Endocytosis experiments

Antibody against EEA1 was purchased from BD Biosciences (Catalog no. 610456). Conjugated transferrin (mouse)-Alexa546, dextran-Alexa555, and EGF-Alexa555 were purchased from Invitrogen. Cy3-conjugated hyaluronate was synthesized in-house. Cy2- or Cy3-conjugated donkey antibodies against mouse IgG were purchased from Jackson ImmunoResearch. For receptor-mediated endocytosis, cells were washed with serum-free medium and then incubated in this medium with Cy3-conjugated hyaluronate (0.1 mg/ml), Alexa 555-conjugated EGF (either 2 ng/ml or 200 ng/ml), or Alexa 546-conjugated transferrin (5 µg/ml) for 1 hr at 4° C. Cells were then washed to

clear unbound ligand, and shifted to 37 °C for times indicated in the figures. Cells were stained for EEA1, followed by confocal microscopy to assess the arrival of ligand to the early endosome. To assess fluid-phase uptake, Alexa 555-conjugated dextran (0.2 mg/ml) was added to complete medium and cells were incubated 37 °C for times indicated in the figures. Cells were then stained for EEA1, followed by confocal microscopy to assess the arrival of this probe to the early endosome.

Confocal microscopy

Colocalization studies were performed with the Zeiss Axio Observer Z1 Inverted Microscope having a Plan-Apochromat 63x objective, the Zeiss LSM 800 with Airyscan confocal package with Zeiss URGB (488- and 561-nm) laser lines, and Zen 2.3 blue edition confocal acquisition software. For quantification of colocalization, ten fields of cells were examined, with each field typically containing about 5 cells. Images were imported into the NIH ImageJ v.1.50e software, and then analyzed through a plugin software (https://imagej.net/Coloc_2). Under the 'image' tab, the 'split channels' option was selected. Under the 'plugins' tab, 'colocalization analysis' option was selected, and within this option, the 'colocalization threshold' option was selected. Menders Coefficient was used for colocalization analysis. Colocalization values were calculated by the software and expressed as the fraction of protein of interest colocalized with EEA1. Colocalization experiments were performed at least twice, and representative data is shown.

Mammosphere Assay

Mammospheres were generated in accordance to a previously described protocol with minor modifications[110]. Briefly, single cell suspensions containing 1,200 WT or AGPS KO pB3 cells were plated in DMEM/F12 supplemented with 2nM L-glutamine, 20ng/mL recombinant human epidermal growth factor (EGF; Peprotech Cat. No. AF-100-15), and B27 supplement (Gibco, Cat. No. 17504-044) in individual wells of an ultra-low attachment 6 well plate (Corning Cat. No. 3471). After 4 days, the total number of spheres greater than 40 µm were quantified before dissociation in trypsin at 37°C. Dissociated cells were then passed through a 40 µm cell strainer to yield a single cell suspension, before replating 1,200 cells. Sphere formation efficiency ((# of mammospheres per well) / (# of cells seeded per well) x 100) was calculated over 3 passages. Data shown is representative of 3 independent biological replicates.

Synthesis of HA-Cy3 probe

Hyaluronic acid (HA, 2 mg, Sigma 75044, Lot #BCBM2884) was dissolved in a 1:1 solution of dimethylsulfoxide (DMSO) and water (0.4 mL) for a stock concentration of 5 mg/mL. The polymer was sonicated under heating to ensure full solubilization. The HA solution was then diluted into HEPES (50 mM final HEPES concentration for a total reaction volume of 2 mL once all components are combined). Sulfo-Cyanine3 amine (2.36 mg, Lumiprobe) was separately dissolved in DMSO (0.236 mL) for a stock concentration of 10 mg/mL. N-(3-Dimethylaminopropyl)-N′-ethylcarbodiimide hydrochloride (EDC, 0.253 mg, Sigma) was separately dissolved in 50 mM HEPES (0.051 mL) for a stock concentration of 5 mg/mL. The HA and EDC solutions were then combined under stirring, followed by addition of the dye solution. The reaction was

stirred, protected from light, at room temperature for 12 h. Following, unreacted dye was removed via Amicon Ultra-0.5 Centrifugal Filters (Millipore Sigma). Manufacturer guidelines were followed to select purification spin speeds and times: 14000 rcf, 15 min per wash step (water) until washes were clear and colorless. The purified HA-Cy3 probe was stored in water at 4 °C until used.

Preparation of liposomes

Ether lipid liposomes were prepared as previously described[22]. PE (18:1p_20:4) (Catalog no. 852804), PE (18:1p_18:1) (Catalog no. 852758), PC (18:1p_20:4) (Catalog no. 852469) and PE (18:0_20:4) (Catalog no. 850804) were purchased from Avanti Polar Lipids Inc.

Characterization of liposomes

Table showing the hydrodynamic diameter and polydispersity of liposomes used in this study. The average and standard deviation of three technical repeats is provided. A Malvern ZS90 Particle Analyzer was used for size measurements reported.

Liposome	Hydrodynamic diameter (nm)	Polydispersity index
PE (18:1p_20:4)	174.8 ± 2.25	0.273 ± 0.01
PE (18:1p_18:1)	128.7 ± 2.07	0.287 ± 0.03
PC (18:1p_20:4)	146.8 ± 1.52	0.21 ± 0.002
PE (18:0_20:4)	182.0 ± 0.13	0.181 ± 0.02

Liposome reconstitution assays

Adherent cells were treated with liposomes 16-18 h prior to performing respective membrane tension or endocytosis assays. Lipid liposomes were added directly to the culture medium for a final concentration of 20 µM. Cells were switched from liposome-containing media to extracellular imaging buffer (HEPES buffer with dextrose, NaCl, KCl, MgCl2, CaCl2) during membrane tension experiments.

Preparation of BSA conjugated DHA (C22:6)

In brief, BSA (FA-free; Fisher Scientific BP9704100) was dissolved in ddH2O to give a 1 mM solution. Exactly 25 mg of docosahexaenoic acid (DHA, C22:6; Sigma Aldrich D2534) was added to 38.05 mL of 1 mM BSA solution to yield a 2:1 DHA:BSA ratio in a glass vial. The vial was then purged with nitrogen and stirred at room temperature until dissolved. The conjugate was then filter sterilized and concentration verified via BCA assay. Aliquots were then stored at -80C until use.

Membrane tension

Tether pulling experiments were performed on a home-built optical trap, following principles described elsewhere[74, 111]. Briefly, 4 µm anti-Digoxigenin-coated polystyrene beads (Spherotech) were trapped with a 1064 nm, Ytterbium laser (IPG Photonics) focused through a 60x 1.2 NA objective (Olympus). Forces on the beads were measured by the deflection of backscattered trapping laser light onto a lateral effect

position sensor (Thorlabs) and calibrated using the viscous drag method[112]. To measure tether radii (R), cell lines were transiently transfected with a membrane-targeted fluorescent protein (glycosylphosphatidylinositol-anchored eGFP, Addgene #32601) using a TransIT-X2 transfection kit (Mirus). Tether radius was obtained by comparing tether fluorescence to fluorescence counts from a known area of the parent cell membrane, as described[59]. Tether force (f) and fluorescence measurements were performed simultaneously. Membrane tension was calculated using the following equation:

$$\text{Membrane tension, } \sigma = \frac{f}{4\pi R}$$

Miscibility transition temperatures (T_{misc}) measurements

Miscibility transition temperatures (T_{misc}) measurements were performed as previously reported[102, 113]. Briefly, cells were washed in PBS, and cell membranes were labeled with 5 µg/ml fluorescent disordered/nonraft phase marker FAST DiO (Thermo Fisher Scientific) for 10 min on ice. Cells were then washed twice in GPMV buffer (10 mM HEPES, 150 mM NaCl, 2 mM CaCl2, pH 7.4), and then incubated with GPMV buffer supplemented with 25 mM paraformaldehyde (PFA) and 2 mM dithiothreitol (DTT) for 1 h at 37 °C. Vesicles were imaged at 40× on an inverted epifluorescence microscope (Leica DMi8) under temperature-controlled conditions using a microscope stage equipped with a Peltier element (Warner Instruments). GPMVs were imaged from 4° C-28 °C, counting phase-separated and uniform vesicles at each temperature. For each temperature, 25-50 vesicles were counted, and the percent of phase-separated vesicles were calculated, plotted versus temperature, and a fitted to a sigmoidal curve to determine the temperature at which 50% of the vesicles were phase-separated (T_{misc}).

C-laurdan spectral imaging

C-Laurdan imaging was performed as previously described[102, 113-116]. Briefly, cells were washed with PBS and stained with 10 µg/mL C-Laurdan for 10 min on ice, then imaged using confocal microscopy on a Leica SP8 with spectral imaging at 60× (water immersion, NA= X) and excitation at 405 nm. The emission was collected as two images: 420–460 nm and 470–510 nm. MATLAB (MathWorks, Natick, MA) was used to calculate the two-dimensional (2D) GP map, where GP for each pixel was calculated as previously described [116]. Briefly, each image was background subtracted and thresholded to keep only pixels with intensities greater than 3 standard deviations of the background value in both channels. The GP image was calculated for each pixel using Equation 1, where G is the G-factor. The G-factor was determined before each experiment using the protocol in[117]. GP maps (pixels represented by GP value rather than intensity) were imported into ImageJ. To calculate the average PM GP, line scans drawn across individual cells. PM GP values were taken as peak GP values from the periphery of the cell, whereas internal membranes were calculated as the average of all values outside the PM peak. The average GP of the internal membranes was calculated by determining the average GP of all pixels in a mask drawn on each cell just inside of the PM.

Equation 1: $GP = \frac{\sum_{420}^{460} I_x - G \sum_{470}^{510} I_x}{\sum_{420}^{460} I_x + G \sum_{470}^{510} I_x}$

Extravasation assay

Cells and reagents

Immortalized human umbilical vein endothelial cells (ECs) expressing BFP[91] were cultured in VascuLife VEGF Endothelial Medium (Lifeline Cell Technology). Normal human lung fibroblasts (FBs) (Lonza, P7) were cultured in FibroLife S2 Fibroblast Medium (Lifeline Cell Technology).

Microfluidic device

3D cell culture chips (AIM Biotech) were used to generate in vitro microvascular networks (MVNs). The AIM chip body was made of cyclic olefin polymer (COP) with a type of gas-permeable plastic serving as the bottom film. AIM Biotech chips contained three parallel channels: a central gel channel flanked by two media channels. Microposts separated fluidic channels and serve to confine the liquid gelling solution in the central channel by surface tension before polymerization. The gel channel was 1.3 mm wide and 0.25 mm tall, the gap between microposts was 0.1 mm, and the width of media channels was 0.5 mm.

Microvascular network formation

To generate perfusable MVNs, ECs and FBs were seeded into the microfluidic chip using a two-step method[118]. Briefly, ECs and FBs were concentrated in VascuLife containing thrombin (4 U/mL). For the first step seeding, the outer layer EC solution was made with a final concentration of 10 $\times 10^6$/mL. After mixed with fibrinogen (3 mg/mL final concentration) at a 1:1 ratio, the outer layer EC solution was pipetted into the gel inlet, immediately followed by aspirating from the gel outlet, leaving only residual solution around the microposts. For the second step, another solution with final concentrations of 5 $\times 10^6$/mL ECs and 1.5 $\times 10^6$/mL fibroblasts were similarly mixed with fibrinogen and then pipetted into the same chip through the gel outlet. The device was placed upside down to polymerize in a humidified enclosure and allowed to polymerize at 37 °C for 15 min in a 5% CO_2 incubator. Next, VascuLife culture medium was added to the media channels and changed daily in the device. After 7 days, MVNs were ready for further experiments.

Tumor cell perfusion in MVNs

PyMT-1099 or pB3 cell line derivatives expressing pCDH-EF1-Luc2-P2A-tdTomato (Plasmid #72486, Addgene) were resuspended at a concentration of 1×10^6/mL in culture medium. To perfuse these tumor cells into in vitro MVNs, the culture medium in one media channel was aspirated, followed by injection of a 20 µL tumor cell suspension in the MVNs and repeated twice. Microfluidic devices were then placed at 37 °C for 15 min in a 5% CO_2 incubator for 15 min. After that, the tumor cell medium was aspirated from the media channels to remove the unattached cells, and Vasculife was replenished. Devices were then placed back to the incubator. 24 h later, devices were fixed, washed, and imaged using an Olympus FLUOVIEW FV1200 confocal laser

scanning microscope with a 10× objective and an additional 2× zoom-in function. Z-stack images were acquired with a 5 µm step size. All images shown are collapsed Z-stacks, displayed using range-adjusted Imaris software, unless otherwise specified. Extravasation percentage was calculated by dividing the cell number of extravasated tumor cells with the total number of tumor cells in the same imaging region of interest.

CLIC/GEEC and micropinocytosis inhibition
7-keto-cholesterol was obtained from Cayman Chemical (Cat. 16339). Cytochalasin D was obtained from Sigma Aldrich (C8273). pB3 cells were pre-treated for 30 minutes with either of the inhibitors before assessing endocytic rate.

RNA interference
In brief, cells were seeded in 6-well plates at the density of 2×10^5 cells/well and transfected 24hr later with the specified siRNA using jetPRIME (Polyplus, 114-15), or PepMute™ (SignaGen, Cat. SL100566) according to the manufacturer's protocol with 100 nM siRNA. The medium was replaced after 6 h. Analysis was performed 72 h after transfection. Suitable small interfering RNAs were designed by Dharmacon for specific down-regulation of PICK1 (5'-cuuagacuaugacaucgaa-3) and CtBP1 (5'-ugucucaucugcuugacagu-3).

Flow Cytometry
MCF7 cells were washed with ice-cold PBS. For antibody staining, cells were incubated with Fc block (Human TruStain FcX, Biolegend, 422302, 1:20) for 15 min, then incubated with the following antibodies: CD24-BV605 (Biolegend, 311124) and CD44-AF647 (Novus Biologicals, NB500-481AF647) in ice cold 10% FBS, PBS, 2 mM EDTA for 20 min at 4 °C and then washed with PBS and resuspended in 10% FBS, PBS, 2 mM EDTA before analysis using a Attune flow cytometer. Data were analyzed with FlowJo software v. 10.10.0.

Histology
Harvested tissues were fixed by incubating with 10% neural-buffered formalin (VWR Scientific) at 4°C for 16–18 h. Fixed samples were then transferred to 70% ethanol and submitted to Hope Babette Tang Histology Facility at the Koch Institute at MIT for paraffin-embedding and H&E staining. Metastatic burden was quantified using QuPath software[119] and Image J[120].

Statistical Analysis
For statistical analyses, Mann-Whitney U test, two-tailed t-test, and one way ANOVA with either Dunnett, Tukey, or Holm-Šídák multiple test corrections were performed using GraphPad Prism Version 10.4.1. Permutation ANOVA was performed in R (v4.4.2) using the *coin* package with 10,000 permutations[121]. Planned contrasts were tested with one-sided Welch's *t*-tests (t.test, base R), and exploratory pairwise comparisons were adjusted for multiple testing using Holm's method (p.adjust).

Data availability: Lipidomic analysis of ether-lipid-deficient cells is provided in supplementary data 1. All other data is provided within source data.

Correspondence and requests for materials should be addressed to: Raphaël Rodriguez, PhD (raphael.rodriguez@curie.fr), Robert A. Weinberg, PhD (weinberg@wi.mit.edu) and Whitney S. Henry, PhD (wshenry@mit.edu).

REFERENCES

1. Levental, I. & Lyman, E. Regulation of membrane protein structure and function by their lipid nano-environment. *Nat Rev Mol Cell Biol* **24**, 107–122 (2023).
2. Viswanathan, V.S. *et al.* Dependency of a therapy-resistant state of cancer cells on a lipid peroxidase pathway. *Nature* **547**, 453–457 (2017).
3. Hangauer, M.J. *et al.* Drug-tolerant persister cancer cells are vulnerable to GPX4 inhibition. *Nature* **551**, 247–250 (2017).
4. Mai, T.T. *et al.* Salinomycin kills cancer stem cells by sequestering iron in lysosomes. *Nat Chem* **9**, 1025–1033 (2017).
5. Stockwell, B.R. *et al.* Ferroptosis: A Regulated Cell Death Nexus Linking Metabolism, Redox Biology, and Disease. *Cell* **171**, 273–285 (2017).
6. Dixon, S.J. *et al.* Ferroptosis: an iron-dependent form of nonapoptotic cell death. *Cell* **149**, 1060–1072 (2012).
7. Caneque, T. *et al.* Activation of lysosomal iron triggers ferroptosis in cancer. *Nature* **642**, 492–500 (2025).
8. Yang, W.S. & Stockwell, B.R. Ferroptosis: Death by Lipid Peroxidation. *Trends Cell Biol* **26**, 165–176 (2016).
9. Gupta, P.B. *et al.* Identification of selective inhibitors of cancer stem cells by high-throughput screening. *Cell* **138**, 645–659 (2009).
10. Antoszczak, M. *et al.* Iron-Sensitive Prodrugs That Trigger Active Ferroptosis in Drug-Tolerant Pancreatic Cancer Cells. *J Am Chem Soc* **144**, 11536–11545 (2022).
11. Yang, W.S. *et al.* Regulation of ferroptotic cancer cell death by GPX4. *Cell* **156**, 317–331 (2014).
12. Doll, S. *et al.* FSP1 is a glutathione-independent ferroptosis suppressor. *Nature* **575**, 693–698 (2019).
13. Bersuker, K. *et al.* The CoQ oxidoreductase FSP1 acts parallel to GPX4 to inhibit ferroptosis. *Nature* **575**, 688–692 (2019).
14. Yang, W.S. & Stockwell, B.R. Synthetic lethal screening identifies compounds activating iron-dependent, nonapoptotic cell death in oncogenic-RAS-harboring cancer cells. *Chem Biol* **15**, 234–245 (2008).
15. Dixon, S.J. *et al.* Pharmacological inhibition of cystine-glutamate exchange induces endoplasmic reticulum stress and ferroptosis. *Elife* **3**, e02523 (2014).
16. Wang, W. *et al.* CD8(+) T cells regulate tumour ferroptosis during cancer immunotherapy. *Nature* **569**, 270–274 (2019).
17. Liang, Y., Zhao, Y., Qi, Z., Li, X. & Zhao, Y. Ferroptosis: CD8(+)T cells' blade to destroy tumor cells or poison for self-destruction. *Cell Death Discov* **11**, 128 (2025).

18. Li, Q. *et al.* Inhibition of neuronal ferroptosis protects hemorrhagic brain. *JCI Insight* **2**, e90777 (2017).
19. Fang, X. *et al.* Ferroptosis as a target for protection against cardiomyopathy. *Proc Natl Acad Sci U S A* **116**, 2672–2680 (2019).
20. Yu, Y. *et al.* Hepatic transferrin plays a role in systemic iron homeostasis and liver ferroptosis. *Blood* **136**, 726–739 (2020).
21. Friedmann Angeli, J.P. *et al.* Inactivation of the ferroptosis regulator Gpx4 triggers acute renal failure in mice. *Nat Cell Biol* **16**, 1180–1191 (2014).
22. Zou, Y. *et al.* Plasticity of ether lipids promotes ferroptosis susceptibility and evasion. *Nature* (2020).
23. Dean, J.M. & Lodhi, I.J. Structural and functional roles of ether lipids. *Protein Cell* **9**, 196–206 (2018).
24. Benjamin, D.I. *et al.* Ether lipid generating enzyme AGPS alters the balance of structural and signaling lipids to fuel cancer pathogenicity. *Proc Natl Acad Sci U S A* **110**, 14912–14917 (2013).
25. Snyder, F. & Wood, R. Alkyl and alk-1-enyl ethers of glycerol in lipids from normal and neoplastic human tissues. *Cancer Res* **29**, 251–257 (1969).
26. Albert, D.H. & Anderson, C.E. Ether-linked glycerolipids in human brain tumors. *Lipids* **12**, 188–192 (1977).
27. Snyder, F., Blank, M.L. & Morris, H.P. Occurrence and nature of O-alkyl and O-alk-I-enyl moieties of glycerol in lipids of Morris transplanted hepatomas and normal rat liver. *Biochim Biophys Acta* **176**, 502–510 (1969).
28. Cui, W., Liu, D., Gu, W. & Chu, B. Peroxisome-driven ether-linked phospholipids biosynthesis is essential for ferroptosis. *Cell Death Differ* **28**, 2536–2551 (2021).
29. Saxena, M., Kalathur, R.K.R., Neutzner, M. & Christofori, G. PyMT-1099, a versatile murine cell model for EMT in breast cancer. *Sci Rep* **8**, 12123 (2018).
30. Doll, S. *et al.* ACSL4 dictates ferroptosis sensitivity by shaping cellular lipid composition. *Nat Chem Biol* **13**, 91–98 (2017).
31. Kagan, V.E. *et al.* Oxidized arachidonic and adrenic PEs navigate cells to ferroptosis. *Nat Chem Biol* **13**, 81–90 (2017).
32. Ye, X. *et al.* Distinct EMT programs control normal mammary stem cells and tumour-initiating cells. *Nature* **525**, 256–260 (2015).
33. Pantopoulos, K., Porwal, S.K., Tartakoff, A. & Devireddy, L. Mechanisms of mammalian iron homeostasis. *Biochemistry* **51**, 5705–5724 (2012).
34. Muckenthaler, M.U., Rivella, S., Hentze, M.W. & Galy, B. A Red Carpet for Iron Metabolism. *Cell* **168**, 344–361 (2017).
35. Muller, S. *et al.* CD44 regulates epigenetic plasticity by mediating iron endocytosis. *Nat Chem* **12**, 929–938 (2020).
36. Niwa, M., Hirayama, T., Okuda, K. & Nagasawa, H. A new class of high-contrast Fe(II) selective fluorescent probes based on spirocyclized scaffolds for visualization of intracellular labile iron delivered by transferrin. *Org Biomol Chem* **12**, 6590–6597 (2014).
37. Houk, R.S. Mass spectrometry of inductively coupled plasmas. *Analytical Chemistry* **58**, 97A–105A (1986).
38. Figueroa, J.A., Stiner, C.A., Radzyukevich, T.L. & Heiny, J.A. Metal ion transport quantified by ICP-MS in intact cells. *Sci Rep* **6**, 20551 (2016).

39. Solier, S. *et al.* A druggable copper-signalling pathway that drives inflammation. *Nature* **617**, 386–394 (2023).
40. Haley, J. *et al.* Functional characterization of a panel of high-grade serous ovarian cancer cell lines as representative experimental models of the disease. *Oncotarget* **7**, 32810–32820 (2016).
41. Hoepken, H.H., Korten, T., Robinson, S.R. & Dringen, R. Iron accumulation, iron-mediated toxicity and altered levels of ferritin and transferrin receptor in cultured astrocytes during incubation with ferric ammonium citrate. *J Neurochem* **88**, 1194–1202 (2004).
42. Bauckman, K.A., Haller, E., Flores, I. & Nanjundan, M. Iron modulates cell survival in a Ras- and MAPK-dependent manner in ovarian cells. *Cell Death Dis* **4**, e592 (2013).
43. Gammella, E., Buratti, P., Cairo, G. & Recalcati, S. The transferrin receptor: the cellular iron gate. *Metallomics* **9**, 1367–1375 (2017).
44. Al-Hajj, M., Wicha, M.S., Benito-Hernandez, A., Morrison, S.J. & Clarke, M.F. Prospective identification of tumorigenic breast cancer cells. *Proc Natl Acad Sci U S A* **100**, 3983–3988 (2003).
45. Yan, Y., Zuo, X. & Wei, D. Concise Review: Emerging Role of CD44 in Cancer Stem Cells: A Promising Biomarker and Therapeutic Target. *Stem Cells Transl Med* **4**, 1033–1043 (2015).
46. Aruffo, A., Stamenkovic, I., Melnick, M., Underhill, C.B. & Seed, B. CD44 is the principal cell surface receptor for hyaluronate. *Cell* **61**, 1303–1313 (1990).
47. Hua, Q., Knudson, C.B. & Knudson, W. Internalization of hyaluronan by chondrocytes occurs via receptor-mediated endocytosis. *J Cell Sci* **106 (Pt 1)**, 365–375 (1993).
48. Bendris, N. *et al.* SNX9 promotes metastasis by enhancing cancer cell invasion via differential regulation of RhoGTPases. *Mol Biol Cell* (2016).
49. Thottacherry, J.J., Sathe, M., Prabhakara, C. & Mayor, S. Spoiled for Choice: Diverse Endocytic Pathways Function at the Cell Surface. *Annu Rev Cell Dev Biol* **35**, 55–84 (2019).
50. Saric, A. & Freeman, S.A. Endomembrane Tension and Trafficking. *Front Cell Dev Biol* **8**, 611326 (2020).
51. McMahon, H.T. & Boucrot, E. Molecular mechanism and physiological functions of clathrin-mediated endocytosis. *Nat Rev Mol Cell Biol* **12**, 517–533 (2011).
52. Sathe, M. *et al.* Small GTPases and BAR domain proteins regulate branched actin polymerisation for clathrin and dynamin-independent endocytosis. *Nat Commun* **9**, 1835 (2018).
53. Rentero, C. *et al.* Functional implications of plasma membrane condensation for T cell activation. *PLoS One* **3**, e2262 (2008).
54. Chaudhary, N. *et al.* Endocytic crosstalk: cavins, caveolins, and caveolae regulate clathrin-independent endocytosis. *PLoS Biol* **12**, e1001832 (2014).
55. Kalin, S. *et al.* Macropinocytotic uptake and infection of human epithelial cells with species B2 adenovirus type 35. *J Virol* **84**, 5336–5350 (2010).
56. Gilleron, J. *et al.* Image-based analysis of lipid nanoparticle-mediated siRNA delivery, intracellular trafficking and endosomal escape. *Nat Biotechnol* **31**, 638–646 (2013).

57. Liberali, P. *et al.* The closure of Pak1-dependent macropinosomes requires the phosphorylation of CtBP1/BARS. *EMBO J* **27**, 970–981 (2008).
58. Brenner, S.L. & Korn, E.D. Substoichiometric concentrations of cytochalasin D inhibit actin polymerization. Additional evidence for an F-actin treadmill. *J Biol Chem* **254**, 9982–9985 (1979).
59. Pinot, M. *et al.* Lipid cell biology. Polyunsaturated phospholipids facilitate membrane deformation and fission by endocytic proteins. *Science* **345**, 693–697 (2014).
60. Galbiati, F., Razani, B. & Lisanti, M.P. Emerging themes in lipid rafts and caveolae. *Cell* **106**, 403–411 (2001).
61. Doherty, G.J. & McMahon, H.T. Mechanisms of endocytosis. *Annu Rev Biochem* **78**, 857–902 (2009).
62. Boucrot, E. *et al.* Endophilin marks and controls a clathrin-independent endocytic pathway. *Nature* **517**, 460–465 (2015).
63. Holst, M.R. *et al.* Clathrin-Independent Endocytosis Suppresses Cancer Cell Blebbing and Invasion. *Cell Rep* **20**, 1893–1905 (2017).
64. Thottacherry, J.J. *et al.* Mechanochemical feedback control of dynamin independent endocytosis modulates membrane tension in adherent cells. *Nat Commun* **9**, 4217 (2018).
65. Baba, T. *et al.* Clathrin-dependent and clathrin-independent endocytosis are differentially sensitive to insertion of poly (ethylene glycol)-derivatized cholesterol in the plasma membrane. *Traffic* **2**, 501–512 (2001).
66. Wu, X.S. *et al.* Membrane Tension Inhibits Rapid and Slow Endocytosis in Secretory Cells. *Biophys J* **113**, 2406–2414 (2017).
67. Gottlieb, T.A., Ivanov, I.E., Adesnik, M. & Sabatini, D.D. Actin microfilaments play a critical role in endocytosis at the apical but not the basolateral surface of polarized epithelial cells. *J Cell Biol* **120**, 695–710 (1993).
68. Dai, J. & Sheetz, M.P. Regulation of endocytosis, exocytosis, and shape by membrane tension. *Cold Spring Harb Symp Quant Biol* **60**, 567–571 (1995).
69. Hirama, T. *et al.* Membrane curvature induced by proximity of anionic phospholipids can initiate endocytosis. *Nat Commun* **8**, 1393 (2017).
70. Loh, J. *et al.* An acute decrease in plasma membrane tension induces macropinocytosis via PLD2 activation. *J Cell Sci* **132** (2019).
71. Bucher, D. *et al.* Clathrin-adaptor ratio and membrane tension regulate the flat-to-curved transition of the clathrin coat during endocytosis. *Nat Commun* **9**, 1109 (2018).
72. Kozlov, M.M. & Chernomordik, L.V. Membrane tension and membrane fusion. *Curr Opin Struct Biol* **33**, 61–67 (2015).
73. Sitarska, E. & Diz-Munoz, A. Pay attention to membrane tension: Mechanobiology of the cell surface. *Curr Opin Cell Biol* **66**, 11–18 (2020).
74. Dai, J. & Sheetz, M.P. Mechanical properties of neuronal growth cone membranes studied by tether formation with laser optical tweezers. *Biophys J* **68**, 988–996 (1995).
75. Levental, K.R. *et al.* Lipidomic and biophysical homeostasis of mammalian membranes counteracts dietary lipid perturbations to maintain cellular fitness. *Nat Commun* **11**, 1339 (2020).

76. Halbleib, K. *et al.* Activation of the Unfolded Protein Response by Lipid Bilayer Stress. *Mol Cell* **67**, 673–684 e678 (2017).
77. Ernst, R., Ejsing, C.S. & Antonny, B. Homeoviscous Adaptation and the Regulation of Membrane Lipids. *J Mol Biol* **428**, 4776–4791 (2016).
78. Levitan, I. Evaluating membrane structure by Laurdan imaging: Disruption of lipid packing by oxidized lipids. *Curr Top Membr* **88**, 235–256 (2021).
79. Thankamony, S.P. & Knudson, W. Acylation of CD44 and its association with lipid rafts are required for receptor and hyaluronan endocytosis. *J Biol Chem* **281**, 34601–34609 (2006).
80. Veatch, S.L. *et al.* Critical fluctuations in plasma membrane vesicles. *ACS Chem Biol* **3**, 287–293 (2008).
81. Li, P. *et al.* The iron chelator Dp44mT suppresses osteosarcoma's proliferation, invasion and migration: in vitro and in vivo. *Am J Transl Res* **8**, 5370–5385 (2016).
82. Basuli, D. *et al.* Iron addiction: a novel therapeutic target in ovarian cancer. *Oncogene* **36**, 4089–4099 (2017).
83. Guo, W. *et al.* An important role of the hepcidin-ferroportin signaling in affecting tumor growth and metastasis. *Acta Biochim Biophys Sin (Shanghai)* **47**, 703–715 (2015).
84. Tsujita, K. *et al.* Homeostatic membrane tension constrains cancer cell dissemination by counteracting BAR protein assembly. *Nat Commun* **12**, 5930 (2021).
85. Chi, Y. *et al.* Cancer cells deploy lipocalin-2 to collect limiting iron in leptomeningeal metastasis. *Science* **369**, 276–282 (2020).
86. Lambert, A.W., Pattabiraman, D.R. & Weinberg, R.A. Emerging Biological Principles of Metastasis. *Cell* **168**, 670–691 (2017).
87. Chen, M.B. *et al.* On-chip human microvasculature assay for visualization and quantification of tumor cell extravasation dynamics. *Nat Protoc* **12**, 865–880 (2017).
88. Chen, M.B., Whisler, J.A., Jeon, J.S. & Kamm, R.D. Mechanisms of tumor cell extravasation in an in vitro microvascular network platform. *Integr Biol (Camb)* **5**, 1262–1271 (2013).
89. Frose, J. *et al.* Epithelial-Mesenchymal Transition Induces Podocalyxin to Promote Extravasation via Ezrin Signaling. *Cell Rep* **24**, 962–972 (2018).
90. Chen, M.B., Lamar, J.M., Li, R., Hynes, R.O. & Kamm, R.D. Elucidation of the Roles of Tumor Integrin beta1 in the Extravasation Stage of the Metastasis Cascade. *Cancer Res* **76**, 2513–2524 (2016).
91. Wan, Z. *et al.* A robust vasculogenic microfluidic model using human immortalized endothelial cells and Thy1 positive fibroblasts. *Biomaterials* **276**, 121032 (2021).
92. Prince, M.E. *et al.* Identification of a subpopulation of cells with cancer stem cell properties in head and neck squamous cell carcinoma. *Proc Natl Acad Sci U S A* **104**, 973–978 (2007).
93. Dontu, G. *et al.* In vitro propagation and transcriptional profiling of human mammary stem/progenitor cells. *Genes Dev* **17**, 1253–1270 (2003).

94. Lambert, A.W. *et al.* DeltaNp63/p73 drive metastatic colonization by controlling a regenerative epithelial stem cell program in quasi-mesenchymal cancer stem cells. *Dev Cell* **57**, 2714–2730 e2718 (2022).
95. Fruman, D.A., Meyers, R.E. & Cantley, L.C. Phosphoinositide kinases. *Annu Rev Biochem* **67**, 481–507 (1998).
96. Rodriguez, R., Schreiber, S.L. & Conrad, M. Persister cancer cells: Iron addiction and vulnerability to ferroptosis. *Mol Cell* (2021).
97. Suzuki, T. *et al.* Crucial role of iron in epigenetic rewriting during adipocyte differentiation mediated by JMJD1A and TET2 activity. *Nucleic Acids Res* (2023).
98. Herr, C.Q. & Hausinger, R.P. Amazing Diversity in Biochemical Roles of Fe(II)/2-Oxoglutarate Oxygenases. *Trends Biochem Sci* **43**, 517–532 (2018).
99. Dongre, A. *et al.* Epithelial-to-Mesenchymal Transition Contributes to Immunosuppression in Breast Carcinomas. *Cancer Res* **77**, 3982–3989 (2017).
100. Hu, Y. & Smyth, G.K. ELDA: extreme limiting dilution analysis for comparing depleted and enriched populations in stem cell and other assays. *J Immunol Methods* **347**, 70–78 (2009).
101. Contag, C.H. & Bachmann, M.H. Advances in in vivo bioluminescence imaging of gene expression. *Annu Rev Biomed Eng* **4**, 235–260 (2002).
102. Levental, K.R. & Levental, I. Isolation of giant plasma membrane vesicles for evaluation of plasma membrane structure and protein partitioning. *Methods Mol Biol* **1232**, 65–77 (2015).
103. Surma, M.A. *et al.* Mouse lipidomics reveals inherent flexibility of a mammalian lipidome. *Sci Rep* **11**, 19364 (2021).
104. Ejsing, C.S. *et al.* Global analysis of the yeast lipidome by quantitative shotgun mass spectrometry. *Proc Natl Acad Sci U S A* **106**, 2136–2141 (2009).
105. Surma, M.A. *et al.* An automated shotgun lipidomics platform for high throughput, comprehensive, and quantitative analysis of blood plasma intact lipids. *Eur J Lipid Sci Technol* **117**, 1540–1549 (2015).
106. Herzog, R. *et al.* A novel informatics concept for high-throughput shotgun lipidomics based on the molecular fragmentation query language. *Genome Biol* **12**, R8 (2011).
107. Herzog, R. *et al.* LipidXplorer: a software for consensual cross-platform lipidomics. *PLoS One* **7**, e29851 (2012).
108. Frolich, N., Klose, C., Widen, E., Ripatti, S. & Gerl, M.J. Imputation of missing values in lipidomic datasets. *Proteomics* **24**, e2300606 (2024).
109. Sampaio, J.L. *et al.* Membrane lipidome of an epithelial cell line. *Proc Natl Acad Sci U S A* **108**, 1903–1907 (2011).
110. Shaw, F.L. *et al.* A detailed mammosphere assay protocol for the quantification of breast stem cell activity. *J Mammary Gland Biol Neoplasia* **17**, 111–117 (2012).
111. Ashkin, A. Acceleration and Trapping of Particles by Radiation Pressure. *Physical Review Letters* **24**, 156–159 (1970).
112. Kuo, S.C. & Sheetz, M.P. Optical tweezers in cell biology. *Trends Cell Biol* **2**, 116–118 (1992).
113. Sezgin, E. *et al.* Elucidating membrane structure and protein behavior using giant plasma membrane vesicles. *Nat Protoc* **7**, 1042–1051 (2012).

114. Levental, K.R. *et al.* Polyunsaturated lipids regulate membrane domain stability by tuning membrane order. *Biophys J* **110(8)**, 1800–1810 (2016).
115. Levental, K.R. *et al.* omega-3 polyunsaturated fatty acids direct differentiation of the membrane phenotype in mesenchymal stem cells to potentiate osteogenesis. *Sci Adv* **3**, eaao1193 (2017).
116. Sezgin, E., Waithe, D., Bernardino de la Serna, J. & Eggeling, C. Spectral imaging to measure heterogeneity in membrane lipid packing. *Chemphyschem : a European journal of chemical physics and physical chemistry* **16**, 1387–1394 (2015).
117. Owen, D.M., Rentero, C., Magenau, A., Abu-Siniyeh, A. & Gaus, K. Quantitative imaging of membrane lipid order in cells and organisms. *Nat Protoc* **7**, 24–35 (2011).
118. Wan, Z. *et al.* A Robust Method for Perfusable Microvascular Network Formation In Vitro. *Small Methods* **6**, e2200143 (2022).
119. Bankhead, P. *et al.* QuPath: Open source software for digital pathology image analysis. *Sci Rep* **7**, 16878 (2017).
120. Schneider, C.A., Rasband, W.S. & Eliceiri, K.W. NIH Image to ImageJ: 25 years of image analysis. *Nat Methods* **9**, 671–675 (2012).
121. Hothorn, T., Hornik, K., van de Wiel, M.A.V. & Zeileis, A. Implementing a Class of Permutation Tests: The coin Package. *J Stat Softw* **28**, 1–23 (2008).

FIGURE LEGENDS

Fig. 1: Ether lipids play a key role in maintaining a ferroptosis susceptible cell state.

a. Schematic of peroxisomal-ether lipid biosynthetic pathway.
b. Cell viability following treatment with the GPX4 inhibitor RSL3 for 72 h. PyMT-1099 WT, AGPS KO, or AGPS addback cells were pretreated with TGF-β (2 ng/ml) for 10 d prior to assay. Data shown as mean +/- SEM. Graph is representative of three independent biological replicates.
c. Bar graph showing percent of total lipids constituted by ether lipids following AGPS KO in untreated wildtype (WT) or TGF-β-treated (2 ng/ml;10 d) PyMT-1099 cells.
d. Pie chart showing the relative proportion of ether lipids with various total numbers of double bonds.

e. Amount in pmol of oxidized phosphatidylethanolamine (Oxi. PE) ether and ester phospholipids in PyMT-1099 TGF-β cells treated with ML210 or vehicle control for 24 h. Five biological replicates per condition. 100,000 cells were used for lipid extraction in each condition. Statistical significance was calculated by unpaired, two-tailed t-test; ns, not significant.
f. Volcano plot showing the $\log_2$ fold change in the relative abundance of various lipid species upon knockout of AGPS in PyMT-1099 TGF-β-treated cells. Blue indicates non-ether linked polyunsaturated phospholipids (PUFA-PLs), red indicates all ether lipids identified in lipidomic analysis and black denotes all other lipids identified.
g. Volcano plot showing the $\log_2$ fold change in the relative abundance of various lipid species upon knockout of AGPS in pB3 cells. Blue indicates non-ether linked polyunsaturated phospholipids (PUFA-PLs), red indicates all ether lipids identified in lipidomic analysis and black denotes all other lipids identified.
h. Bar graph showing the percent of total lipids constituted by ether lipids in pB3 WT, pB3 AGPS KO and pB3 AGPS addback cells.
i. Bar graphs showing the effects of ether lipids on the relative abundance of selected polyunsaturated diacyl phospholipids in pB3 cells.

All lipidomic data were analyzed in triplicate and shown as the mean +/− SEM. Unless otherwise stated statistical significance was calculated by one-way ANOVA with Tukey's multiple comparisons test; ns, not significant. For panel b: PyMT-1099 WT and AGPS KO cells were transduced with the respective vector control plasmids. For panels h-i: pB3 WT and AGPS KO cells were transduced with the respective vector control plasmids.

<u>Fig. 2: Ether lipids regulate cellular redox-active iron levels in cancer cells.</u>

a. Relative lysosomal iron levels based on HRhoNox-M fluorescence intensity normalized to the fluorescence intensity of lysotracker. Fold change is calculated relative to the average of untreated PyMT-1099 wild-type (WT) cells. Statistical significance was calculated by one-way ANOVA with Holm-Šídák multiple comparisons test; ns, not significant.
b. Relative lysosomal iron levels based on HRhoNox-M fluorescence intensity normalized to the fluorescence intensity of lysotracker. Fold change is calculated relative to the average of pB3 WT cells. Statistical significance was calculated by one-way ANOVA with Holm-Šídák multiple comparisons test; ns, not significant.
c. Inductively coupled plasma-mass spectrometry (ICP-MS) of cellular iron in PyMT-1099 WT or AGPS KO cells pretreated with 2 ng/ml TGF-β for 10 d. Statistical significance was calculated by one-way ANOVA with Tukey's multiple comparisons test; ns, not significant.
d. Inductively coupled plasma-mass spectrometry (ICP-MS) of cellular iron in pB3 cell line derivatives. Statistical significance was calculated by one-way ANOVA with Tukey's multiple comparisons test; ns, not significant.
e. Relative lysosomal iron levels in OVCAR8 NT sg, FAR1 KO or AGPS KO cells pretreated with ferric ammonium citrate FAC (50 µg/ml) for 24 h. Data shown are based on HRhoNox-M fluorescence intensity normalized to lysotracker fluorescence intensity. Fold change is calculated relative to the average of NT sg cells. Statistical

significance was calculated by one-way ANOVA with Holm-Šídák multiple comparisons test; ns, not significant.

f. ICP-MS of cellular iron in OVCAR8 NT sg, FAR1 KO or AGPS KO cells pretreated with FAC (50 µg/ml) for 24 h. Statistical significance was calculated by one-way ANOVA with Tukey's multiple comparisons test; ns, not significant.
g. Cell viability of OVCAR8 NT sg, FAR1 KO or AGPS KO cells pretreated with or without FAC (50 µg/ml) for 24 h followed by ML210 treatment for 72 h. Liproxstatin-1 (0.2 µM) was added at the time of ML210. Data representative of 3 independent experiments.
h. Cell viability in response to ML210 treatment. PyMT-1099 WT or AGPS KO cells were pretreated with or without TGF-β (2 ng/ml) for 10 days followed by FAC treatment (100 µg/ml) for an additional 24 h. Cells were then treated with ML210 in the presence or absence of liproxstatin-1 (0.2µM) and cell viability was assessed after 72 h. Data representative of 3 independent experiments.
i. ICP-MS of cellular iron from primary tumors derived from pB3 WT, pB3 AGPS KO, and pB3 AGPS addback cells. Mean +/- SEM from 3 independent tumor samples per condition. Each datapoint represents iron levels from independent tumor samples. Group differences were tested by permutation ANOVA followed by one tailed Welch's t-tests with Holm correction for multiple comparisons.

Unless otherwise noted, all samples were analyzed with 3-6 independent biological replicates and shown as the mean +/− SEM. For panels b, d & i: pB3 WT and AGPS KO cells were transduced with the respective vector control plasmids. Abbreviation: NT – nontargeting.

<u>Fig. 3: Ether lipids facilitate CD44-mediated iron endocytosis.</u>

a. Endocytic transport of fluorescently labeled transferrin as assessed by quantitative colocalization with an early endosomal marker (EEA1) in pB3 WT, AGPS KO, and AGPS addback cells.
b. Endocytic transport of fluorescently labeled hyaluronate probe as assessed by quantitative colocalization with an early endosomal marker (EEA1) in pB3 WT, AGPS KO, and AGPS addback cells.
c. Endocytic transport of fluorescently labeled transferrin as assessed by quantitative colocalization with an early endosomal marker (EEA1) in PyMT-1099 WT or AGPS KO cells pretreated with or without 2 ng/ml TGF-β for 10 d.
d. Endocytic transport of fluorescently labeled hyaluronate probe as assessed by quantitative colocalization with an early endosomal marker (EEA1) in PyMT-1099 WT or AGPS KO cells pretreated with or without 2 ng/ml TGF-β for 10 d.
e. Inductively coupled plasma-mass spectrometry ICP-MS of cellular iron following treatment with either hyaluronic acid or hyaluronidase in PyMT-1099 WT or CD44 KO cells pretreated with or without 2 ng/ml TGF-β for 10 d.
f. Endocytic transport of dextran as assessed by quantitative colocalization with the early endosomal marker EEA1 in pB3 WT, AGPS KO, and AGPS addback cells.
g. Endocytic transport of dextran as assessed by quantitative colocalization with the early endosomal marker EEA1 in PyMT-1099 WT or AGPS KO cells pretreated with or without 2 ng/ml TGF-β for 10 d.

h. Endocytosis of EGFR as assessed by quantitative colocalization of internalized fluorescently labeled EGF with an early endosomal marker (EEA1) in PyMT-1099 WT or AGPS KO cells pretreated with or without 2 ng/ml TGF-β for 10 days. Cells were treated with 2 ng/ml Alexa 555-conjugated EGF.
i. Endocytic transport of hyaluronate-layered nanoparticle assessed by quantitative colocalization of internalized nanoparticles with an early endosomal marker (EEA1) in pB3 WT or AGPS KO cells with or without pre-treatment with polyunsaturated fatty acid (PUFA) BSA conjugate (C22:6).
j. Endocytic transport of hyaluronate-layered nanoparticle assessed by quantitative colocalization of internalized nanoparticles with an early endosomal marker (EEA1) in pB3 WT or AGPS KO cells pre-treated (16-18 hr) with liposomes composed of the following: PE (18:0_20:4), PE (18:1p_20:4), and PC (18:1p_20:4).

All data shown as mean +/− SEM and statistical significance was calculated by one-way ANOVA with Tukey's multiple comparisons test; ns, not significant. Examined n=10 fields of cells per experimental sample for all endocytosis-related experiments and at least two independent replicates were performed. In some cases, error bars are smaller than the symbol size and not visible. ICP-MS experiments were performed with n=4. For panels a, b & f: pB3 WT and AGPS KO cells were transduced with the respective vector control plasmids.

<u>Fig. 4: Ether lipid deficiency impairs membrane biophysical properties.</u>

a. Schematic of membrane tether pulling assay and fluorescence image showing a tether pulled from the plasma membrane of a pB3 cell using an optically trapped 4 µm anti-Digoxigenin coated polystyrene bead.
b. Graph showing tether radius (R) and tether force measurements (f) in pB3 WT, AGPS KO, and AGPS addback cells. All data shown as mean +/− SD.
c. Membrane tension measurements in pB3 WT, AGPS KO pretreated with 20µM of the indicated ether phospholipid liposomes, and AGPS addback cells. All data shown as mean +/− SEM.
d. Endocytic transport of fluorescently labeled hyaluronate probe as assessed by quantitative colocalization with an early endosomal marker (EEA1) in pB3 WT or AGPS KO cells pretreated with 20µM of the indicated ether phospholipid liposomes. All data shown as mean +/− SEM.
e. Endocytic transport of fluorescently labeled transferrin as assessed by quantitative colocalization with an early endosomal marker (EEA1) in pB3 WT or AGPS KO cells pretreated with 20µM of the indicated ether phospholipid liposomes. All data shown as mean +/− SEM.
f. Generalized polarization (GP) values of C-laurdan-labeled plasma membranes from pB3 WT, AGPS KO and AGPS addback cells. Data is shown as mean GP +/− SD.
g. GP values of C-laurdan-labeled intracellular membranes from pB3 WT, AGPS KO and AGPS addback cells. Data is shown as mean GP +/− SD.
h. GP values of C-laurdan-labeled intracellular membranes from PyMT-1099 WT or AGPS KO cells treated with or without 2 ng/ml TGF-β for 10 d. Data shown as mean GP +/− SD.
i. Representative curves showing giant plasma membrane vesicle (GPMV) phase separation from AGPS KO versus WT pB3 cells. Curves were generated by counting

≥ 20 vesicles/temperature/condition at >4 temperature. The data was fit to a sigmoidal curve to determine the temperature at which 50% of the vesicles were phase-separated (T_{misc}). Data shown as the average fits of 3 independent experiments. Graph shows the mean +/- SD of 3 independent experiments. Inset shows the mean miscibility transition temperatures (T_{misc}) +/− SD upon loss of AGPS in pB3 cells. Statistical significance was calculated using unpaired, two-tailed t-test.

Unless otherwise noted, all data is shown as mean +/− SEM and statistical significance was calculated by one-way ANOVA with Tukey's multiple comparisons test; ns, not significant. Examined n=10 fields of cells per experimental sample for all endocytosis-related experiments and at least two independent replicates were performed. For panels b, c, f & g: pB3 WT and AGPS KO cells were transduced with the respective vector control plasmids.

Fig. 5: Loss of ether lipids decreases metastasis and cancer cell stemness.

a. Representative confocal images of extravasated tdTomato-labeled pB3 WT and AGPS KO cells from an in vitro microvascular network established using HUVEC (green) and normal human lung fibroblasts (unlabeled), over a time period of 24 h.
b. Quantification of extravasated tdTomato-labeled pB3 WT and AGPS KO cells from an in vitro microvascular network established using HUVEC (green) and normal human lung fibroblasts (unlabeled), over a time period of 24 h. Each datapoint represents number of extravasated cells per device. Data is representative of two independent biological replicates. Graph shows the mean +/- SEM and statistical significance was calculated using unpaired, two-tailed t-test.
c. Quantification of extravasated tdTomato-labeled PyMT-1099 cell line derivatives from an in vitro microvascular network established using HUVEC (green) and normal human lung fibroblasts (unlabeled), over a time period of 24 h. Each datapoint represents number of extravasated cells per device. Data is representative of two independent biological replicates. Graph shows the mean +/- SEM and statistical significance was calculated by one-way ANOVA with Tukey's multiple comparisons test; ns, not significant.
d. Representative in vivo imaging system (IVIS) images of overall metastatic burden in C57BL/6 female mice following intracardiac injection of GFP-luciferized pB3 WT (n=5) and AGPS KO (n=5) cells.
e. Quantification of overall metastatic burden in C57BL/6 female mice following intracardiac injection of GFP-luciferized pB3 WT (n=5) and AGPS KO (n=5) cells. Graph shows the mean +/- SEM and statistical significance was calculated using Mann-Whitney test.
f. Representative images of H&E-stained sections of harvested kidneys from C57BL/6 female mice following intracardiac injection of pB3 WT or pB3 AGPS KO cells.
g. Gross images of primary tumors derived from pB3 WT control cells and pB3 AGPS KO cells.
h. Tumor growth kinetics of primary tumors derived from pB3 WT control cells and pB3 AGPS KO cells. (n=5 mice per group). Data shown as mean +/- SEM.
i. Bar graph showing the average weight from primary tumors derived from pB3 WT control cells and pB3 AGPS KO cells. Graph shows the mean +/- SEM and statistical significance was calculated using Mann-Whitney test; ns, not significant.

j. Estimated number of cancer stem cells (CSCs) per 10,000 cells as calculated by extreme limiting dilution analysis (ELDA) software. Tumor-initiating capacity was assessed following implantation of indicated amounts of pB3 WT or pB3 AGPS KO cells into the mammary fat pad of C57BL/6 mice. *P* values, $\chi 2$ pairwise test.
k. Table showing the number of mice with palpable primary tumors at 121 d post orthotopic implantation of PyMT-1099 WT or AGPS KO cells pretreated with or without 2 ng/ml TGF-β for 10 d into NSG female mice.
l. Quantification of lung metastases for aforementioned experiment. Data shows the mean number of lung metastases +/- SEM. Statistical significance was calculated by one-way ANOVA with Tukey's multiple comparisons test; ns, not significant.
m. Representative images of H&E-stained lungs harvested from female NSG mice following orthotopic injection of PyMT-1099 WT or AGPS KO cells pretreated with or without 2 ng/ml TGF-β for 10 d. Lungs were harvested after 121 d post-injection. Arrows indicate metastases.

EXTENDED DATA FIGURE LEGENDS

Extended Data Fig. 1

a. Immunoblot analysis for EMT markers and TGF-β signaling in PyMT-1099 WT or AGPS KO cells. Where indicated cells were treated with TGF-β (2 ng/ml) for 10 d.
b. Cell viability following treatment with the GPX4 inhibitor ML210 for 72 h. PyMT-1099 WT or AGPS KO cells were pretreated with TGF-β (2 ng/ml) for 10 d prior to assay. Graph is representative of three independent biological replicates. Data shown as mean +/- SEM.
c. Amount in pmol of oxidized phosphatidylethanolamine (Oxi. PE) ether and ester phospholipids in pB3 cells treated with RSL3 or vehicle control for 24 hours. Five biological replicates per condition. 100,000 cells were used for lipid extraction in each condition. Data shown as mean +/- SEM. Statistical significance was calculated using unpaired, two-tailed t-test.
d. Immunoblot analysis for AGPS expression in mesenchymal-enriched pB3 WT, AGPS KO, and AGPS addback cells. pB2 cells served as a control for expression of epithelial-like markers.

For panel a: PyMT-1099 WT and AGPS KO cells were transduced with the respective vector control plasmids. For panel d: pB3 WT and AGPS KO cells were transduced with the respective vector control plasmids.

Extended Data Fig. 2

a. Relative abundance of lipid classes in PyMT-1099 WT and AGPS KO cells treated with TGF-β (2 ng/ml, 10 d). Lipid classes include triacylglycerol (TAG), sphingomyelin (SM), phosphatidylserine (PS), phosphatidylinositol (PI), phosphatidylglycerol (PG), phosphatidylethanolamine (PE), ether phosphatidylethanolamine (PE O-), phosphatidylcholine (PC), ether phosphatidylcholine (PC O-), phosphatidic acid (PA), lysophosphatidylserine (LPS), lysophosphatidylinositol (LPI), lysophosphatidylglycerol (LPG), lysophosphatidylethanolamine (LPE), lysophosphatidylcholine (LPC), ether

lysophosphatidylethanolamine (LPEO-), ether lysophosphatidylcholine (LPCO-), lysophosphatidic acid (LPA), hexosylceramide (HexCer), diacylglycerol (DAG), cardiolipin (CL), ceramide (Cer), and cholesteryl ester (CE).

b. Bar plot showing the distribution of saturation levels (total number of double bonds) among membrane lipid species present in PyMT-1099 WT and AGPS KO cells treated with TGF-β (2 ng/ml, 10 d).
c. Quantification of the relative abundance of non-ether polyunsaturated phosphatidylethanolamine (PUFA PE) species in PyMT-1099 WT and AGPS KO cells treated with TGF-β (2 ng/ml, 10 d).
d. Quantification of the relative abundance of non-ether polyunsaturated phosphatidylcholine (PUFA PC) species in PyMT-1099 WT and AGPS KO cells treated with TGF-β (2 ng/ml, 10 d).

All data shown as the mean +/− SEM of 3 replicates. Statistical significance was calculated using unpaired, two-tailed t-test.

Extended Data Fig. 3

a. Relative abundance of lipid classes in WT, AGPS KO, and AGPS addback pB3 cells. Lipid classes include triacylglycerol (TAG), sphingomyelin (SM), phosphatidylserine (PS), phosphatidylinositol (PI), phosphatidylglycerol (PG), phosphatidylethanolamine (PE), ether phosphatidylethanolamine (PE O-), phosphatidylcholine (PC), ether phosphatidylcholine (PC O-), phosphatidic acid (PA), lysophosphatidylserine (LPS), lysophosphatidylinositol (LPI), lysophosphatidylglycerol (LPG), lysophosphatidylethanolamine (LPE), lysophosphatidylcholine (LPC), ether lysophosphatidylethanolamine (LPEO-), ether lysophosphatidylcholine (LPCO-), lysophosphatidic acid (LPA), hexosylceramide (HexCer), diacylglycerol (DAG), cardiolipin (CL), ceramide (Cer), and cholesteryl ester (CE).
b. Hierarchical clustering heatmap of polyunsaturated phosphatidylethanolamine (PUFA PE) species based on abundance (mol% of total lipids) in WT, AGPS KO, and AGPS addback pB3 cells. A sample variance of greater than 10 was used as a filter for representing species within the heatmap.
c. Hierarchical clustering heatmap of polyunsaturated phosphatidylcholine (PUFA PC) species based on abundance (mol% of total lipids) in WT, AGPS KO, and AGPS addback pB3 cells. A sample variance of greater than 10 was used as a filter for representing species within the heatmap.
d. Bar plot quantifying the relative abundance of non-ether PUFA PC species in WT, AGPS KO, and AGPS addback pB3 cells.
e. Bar plot quantifying the relative abundance of non-ether PUFA PE species in WT, AGPS KO, and AGPS addback pB3 cells.
f. Bar plot showing the distribution of saturation levels (total number of double bonds) among membrane lipid species present in WT, AGPS KO, and AGPS addback pB3 cells.

All samples were analyzed with 3 biological replicates and represented as the mean +/− SEM. Statistical significance was calculated using one-way ANOVA with Tukey's multiple comparisons test; ns, not significant. pB3 WT and AGPS KO cells were transduced with the respective vector control plasmids.

Extended Data Fig. 4

a. ICP-MS of cellular iron in the mesenchymal-enriched 687g WT and AGPS KO murine breast cancer cell line. All shown as the mean +/− SEM of 3 replicates. Statistical significance was calculated using unpaired, two-tailed t-test.
b. Immunoblot analysis of OVCAR8 AGPS KO, FAR1 KO or nontargeting sg (WT) cells.

Extended Data Fig. 5

a. Representative confocal images showing internalization of transferrin (red) and colocalization with the early endosome marker EEA1 (green) at 0, 2, and 5 minutes in WT, AGPS KO, and AGPS addback pB3 cells. Scale bar: 10 µm.
b. Representative confocal images showing internalization of fluorescently labeled hyaluronate probe (red) and colocalization with EEA1 (green) at 0, 10, 30, and 60 minutes in WT, AGPS KO, and AGPS addback pB3 cells. Scale bar: 10 µm.
c. Representative confocal images of transferrin (red) and EEA1 (green) colocalization at 0, 2, and 5 minutes in WT and AGPS KO PyMT-1099 cells +/- TGF-β pre-treatment (2 ng/ml; 10 d). Scale bar: 10 µm.
d. Representative confocal images showing internalization of fluorescently labeled hyaluronate probe (red) and EEA1 (green) at 0, 10, 30, and 60 minutes in WT and AGPS KO PyMT-1099 cells +/- TGF-β pre-treatment (2 ng/ml; 10 d). Scale bar: 10 µm.
e. Representative confocal images showing dextran (red) internalization and colocalization with EEA1 (green) at 0, 2, and 5 minutes in WT, AGPS KO, and AGPS addback pB3 cells. Scale bar: 10 µm.
f. Representative confocal images of dextran (red) and EEA1 (green) at 0, 5, and 20 minutes in WT and AGPS KO PyMT-1099 cells +/- TGF-β pre-treatment (2 ng/ml; 10 d). Scale bar: 10 µm.

For panels a, b & e: pB3 WT and AGPS KO cells were transduced with the respective vector control plasmids. Examined n=10 fields of cells per experimental sample and at least two independent replicates were performed.

Extended Data Fig. 6

a. Representative confocal images showing EGF (red) internalization and colocalization with EEA1 (green) at 0, 2, and 5 minutes in WT and AGPS KO PyMT-1099 cells +/- TGF-β pre-treatment (2 ng/ml; 10 d). Scale bar: 10 µm. Cells were treated with 2 ng/ml Alexa 555-conjugated EGF.
b. Representative confocal images of hyaluronate layered nanoparticle (red) and EEA1 (green) colocalization at 0, 10, 30, and 60 minutes in pB3 WT, AGPS KO, and AGPS KO supplemented with polyunsaturated fatty acid (PUFA) BSA conjugate (C22:6). Scale bar: 10 µm.
c. Representative confocal images of hyaluronate layered nanoparticle (red) and EEA1 (green) colocalization at 0, 10, 30, and 60 minutes in WT, AGPS KO, and AGPS KO pB3 cells pre-treated with the indicated liposome supplementations PE (18:0_20:4), PE (18:1p_20:4), and PC (18:1p_20:4) for 16-18 hr. Scale bar: 10 µm.

d. Representative confocal images of fluorescently labeled hyaluronate probe (red) and EEA1 (green) colocalization at 0, 10, 30, and 60 minutes in WT, AGPS KO, and AGPS KO pB3 cells supplemented with liposomes composed of ether PE species 18:1p_18:1 and 18:1p_20:4. Scale bar: 10 µm.
e. Representative confocal images showing transferrin (red) and EEA1 (green) colocalization at 0, 2, and 5 minutes in WT, AGPS KO, and AGPS KO pB3 cells supplemented with defined ether PE species (18:1p_18:1 and 18:1p_20:4). Scale bar: 10 µm.

Examined n=10 fields of cells per experimental sample for all experiments and at least two independent replicates were performed.

Extended Data Fig. 7

a. Representative confocal images of EGF colocalization with an early endosomal marker (EEA1) in PyMT-1099 WT or AGPS KO cells pretreated with 2 ng/ml TGF-β for 10 days. Cells were treated with 200 ng/ml EGF.
b. Quantification of co-localization EGF as assessed displayed in panel a. All data shown as mean +/- SEM.
c. Representative confocal images of giant plasma membrane vesicles GPMVs budding from WT, AGPS KO, and AGPS addback pB3 cells stained with FAST DiO dye. Scale bars: 10 µm.
d. Quantification of membrane tension in pB3 WT and CD44 KO. All data shown as mean +/− SEM. Statistical significance was calculated using unpaired, two-tailed t-test.
e. Graph showing tether radius (R) and tether force measurements (f) in pB3 WT and CD44 KO cells. All data shown as mean +/− SD.
f. Boxplots quantifying total iron content via ICP-MS (ng Fe per 1×10 cells) in WT and CD44 KO OVCAR8 cells treated with hyaluronic acid or hyaluronidase as indicated. Data shown as mean +/− SEM. As this experiment serves as validation of a prior findings, we tested the shown comparisons using one-sided Welch's *t*-tests without multiple-testing correction.

Examined n=10 fields of cells per experimental sample for endocytosis-related experiments. Four independent replicates were measured for ICP-MS data. For panel c: pB3 WT and AGPS KO cells were transduced with the respective vector control plasmids.

Extended Data Fig. 8

a. Immunoblot analysis of CtBP1 and PICK1 protein expression following siRNA-mediated knockdown (siCtBP1, siPICK1) or control siRNA (siCtrl) in pB3 cells. γ-Tubulin serves as a loading control.
b. Scatter plots quantifying lysosomal iron (measured as mean fluorescence intensity, MFI, of HRhoNox-M) in pB3 cells transfected with siCtrl, siCtBP1, or siPICK1 for 72 hr. Each point represents an independent replicate.
c. Scatter plots quantifying lysosomal iron (measured as mean fluorescence intensity, MFI, of HRhoNox-M) in pB3 cells treated with vehicle, cytochalasin D, or 7-keto-cholesterol for 30 minutes. Each point represents an independent replicate.

d. Representative confocal images showing hyaluronate-layered nanoparticle (red) internalization and colocalization with early endosome marker EEA1 (green) at 0, 10, 30, and 60 minutes in WT pB3 cells under the following treatments: no treatment, siCtBP1, and cytochalasin D. Data is representative of at least 2 independent experiments. Scale bar: 10 µm.
e. Representative confocal images showing hyaluronate-layered nanoparticle (red) internalization and colocalization with early endosome marker EEA1 (green) in pB3 cells at 0, 10, 30, and 60 minutes in WT pB3 cells under the following treatments: no treatment, siPICK1, and 7-keto-cholesterol. Data is representative of at least 2 independent experiments. Scale bar: 10 µm.
f. Quantification of the percentage of hyaluronate-layered nanoparticle labeled endosomes colocalized with EEA1 in pB3 cells over time (0–60 min) in the indicated treatment groups: No treatment, siCtBP1, or cytochalasin D. Examined n=10 fields of cells per experimental sample. Data is representative of at least 2 independent experiments.
g. Quantification of the percentage of hyaluronate-layered nanoparticle labeled endosomes colocalized with EEA1 in pB3 cells over time (0–60 min) in the indicated treatment groups: No treatment, siPICK1, or 7-keto-cholesterol. Examined n=10 fields of cells per experimental sample. Data is representative of at least 2 independent experiments.
h. Total iron content (ng Fe per $1x10^6$ cells) in pB3 cells transfected with siCtrl, siCtBP1, or siPICK1 as quantified by ICM-MS. Each point represents an independent replicate.

All data shown as mean +/− SEM and statistical significance was calculated using one-way ANOVA with Dunnett's multiple comparisons test; ns, not significant. In some cases, error bars may be obscured by data points.

<u>Extended Data Fig. 9</u>

a. Bar plot showing the abundance (mol% of total lipids) of each major lipid class in isolated giant plasma membrane vesicles (GPMVs) from WT, AGPS KO and AGPS addback pB3 cells. Lipid classes include diacylglycerol (DAG), sphingomyelin (SM), phosphatidylserine (PS), phosphatidylinositol (PI), phosphatidylglycerol (PG), phosphatidylethanolamine (PE), ether phosphatidylethanolamine (PEO-), phosphatidylcholine (PC), ether phosphatidylcholine (PCO-), phosphatidic acid (PA), lysophosphatidylserine (LPS), lysophosphatidylinositol (LPI), lysophosphatidylethanolamine (LPE), lysophosphatidylcholine (LPC), ether lysophosphatidylethanolamine (LPEO-), ether lysophosphatidylcholine (LPCO-), hexosylceramide (HexCer), cardiolipin (CL), ceramide (Cer), cholesteryl ester (CE), cholesterol (Chol) and triacylglycerol (TAG).
b. Enrichment PS and SM lipid abundance (mol% of total lipids) in WT, AGPS KO, and AGPS addback pB3 derived GPMVs compared to whole cell extracts.
c. Bar plot showing the distribution of relative phospholipid levels according to the total number of double bonds per lipid species in GPMVs derived from WT, AGPS KO, and AGPS addback pB3 cells.
d. Quantification of total ether lipid levels (mol% of total lipids) in WT, AGPS KO, and AGPS addback pB3 derived GPMVs.

e. Volcano plot showing the log_2(fold change) in the relative abundance of various lipid species present in GPMVs upon knockout of AGPS in pB3 cells. Blue indicates non-ether linked polyunsaturated phospholipids; red indicates all ether lipids identified in lipidomic analysis and black denotes all other lipids identified.
f. Quantification of the relative levels (mol% of total lipids) of non-ether polyunsaturated phosphatidylethanolamine or phosphatidylcholine lipids (PC or PE) in WT, AGPS KO, and AGPS addback pB3 cells.

All data shown as mean +/− SEM and statistical significance was calculated using one-way ANOVA with Tukey's multiple comparisons test; ns, not significant. pB3 WT and AGPS KO cells were transduced with the respective vector control plasmids.

Extended Data Fig. 10

a. Bright-field (top) and fluorescence images (bottom) showing mesenteric metastases from athymic nude mice injected with tdTomato-labeled OVCAR8 NT sg, AGPS KO and FAR1 KO cells via the intraperitoneal route.
b. Representative in vivo imaging system (IVIS) images of overall metastatic burden in C57BL/6 female mice following intracardiac injection of GFP-luciferized pB3 WT (n=5) and CD44 KO (n=6) cells.
c. Quantification of overall metastatic burden in C57BL/6 female mice following intracardiac injection of GFP-luciferized pB3 WT (n=5) and CD44 KO (n=6) cells. Data shown as mean +/- SEM. Statistical significance was calculated using the Mann-Whitney test.
d. Bar plot showing the in vitro mammosphere formation efficiency of pB3 WT and AGPS KO cells over three passages. Data is representative of three independent biological replicates. Data shown as mean +/- SEM. Statistical significance was calculated using unpaired, two-tailed t-test.
e. Table showing number of pB3 WT or AGPS KO cells implanted per mouse and number of mice with tumors after 39 days.

Extended Data Fig. 11

a. Immunoblot showing the expression of various EMT markers in MCF7 cells treated with vehicle control or oncostatin M (OSM, 100 ng/mL) for 72 hr. γ-Tubulin serves as a loading control.
b. Representative flow cytometry plots of CD44 (AF647) and CD24 (BV605) staining in MCF7 cells treated with vehicle control or OSM (100 ng/mL) for 72 hr. Percentage of $CD44^{lo}/CD24^{hi}$ cells and $CD44^{hi}/CD24^{lo}$ is indicated. Data is representative of at least two independent experiments.
c. Scatter plot quantifying total iron (ng Fe per 1×10□ cells) in vehicle control or OSM (100 ng/mL; 72 hr) treated MCF7 cells. Each point represents a biological replicate.
d. Bar plot showing the mol% of total lipids for each major lipid class in vehicle control and OSM treated MCF7 cells. Lipid classes include triacylglycerol (TAG), sphingomyelin (SM), phosphatidylserine (PS), phosphatidylinositol (PI), phosphatidylglycerol (PG), phosphatidylethanolamine (PE), ether phosphatidylethanolamine (PEO-), phosphatidylcholine (PC), ether phosphatidylcholine (PCO-), phosphatidic acid (PA), lysophosphatidylserine (LPS), lysophosphatidylinositol (LPI), lysophosphatidylethanolamine (LPE),

lysophosphatidylglycerol (LPG), lysophosphatidylcholine (LPC), ether lysophosphatidylethanolamine (LPEO-), ether lysophosphatidylcholine (LPCO-), lysophosphatidic acid (LPA), hexosylceramide (HexCer), diacylglycerol (DAG), cardiolipin (CL), ceramide (Cer), and cholesteryl ester (CE). Inset shows low abundance lipid species.

e. Relative abundance (mol% of membrane lipids) of individual ether lipid species in vehicle control and OSM treated MCF7 cells (100 ng/mL; 72 hr).
f. Quantification of saturation levels (total number of double bonds) among membrane ether lipid species in vehicle and OSM treated MCF7 cells.
g. Quantification of the levels (mol% of membrane lipids) of ether polyunsaturated fatty acid (PUFA) PE and PC species in vehicle control and OSM treated MCF7 cells (100 ng/mL; 72 hr).

All data shown as mean +/− SEM and unless otherwise noted, statistical significance was calculated using unpaired, two-tailed t-test.

Extended Data Fig. 12

a. Relative abundance of lipid classes in TGF-β-treated (2 ng/ml; 10 d) PyMT-1099 WT cells compared to untreated control. Lipid classes include: triacylglycerol (TAG), sphingomyelin (SM), phosphatidylserine (PS), phosphatidylinositol (PI), phosphatidylglycerol (PG), phosphatidylethanolamine (PE), ether phosphatidylethanolamine (PE O-), phosphatidylcholine (PC), ether phosphatidylcholine (PC O-), phosphatidic acid (PA), lysophosphatidylserine (LPS), lysophosphatidylinositol (LPI), lysophosphatidylethanolamine (LPE), lysophosphatidylcholine (LPC), ether lysophosphatidylethanolamine (LPEO-), ether lysophosphatidylcholine (LPCO-), lysophosphatidylglycerol (LPG), lysophosphatidic acid (LPA), hexosylceramide (HexCer), diacylglycerol (DAG), cardiolipin (CL), ceramide (Cer), and cholesteryl ester (CE). Data shown as mean +/- SEM. Inset shows low abundance lipid species.
b. Bar plot showing the distribution of ether phospholipids +/- SEM according to the number of double bonds per species (mol% of membrane lipids) in WT and TGFβ-treated WT cells. Data shown as mean +/− SEM.
c. Dot plot showing the calculated Log_2(fold change) of ether phospholipids with an adjusted p value less than or equal to 0.02 in PyMT-1099 TGF-β-treated (2 ng/ml; 10 d) cells relative to untreated (Ctrl) cells. Red dots indicate ether phospholipids containing polyunsaturated fatty acids (PUFA) at both sn-1 and sn-2 positions. Blue dot indicates ether phospholipids containing only saturated (SA) or monounsaturated (MUFA) fatty acids at both sn-1 and sn-2 positions. Black dot indicates all other ether phospholipids.

Fig. 1

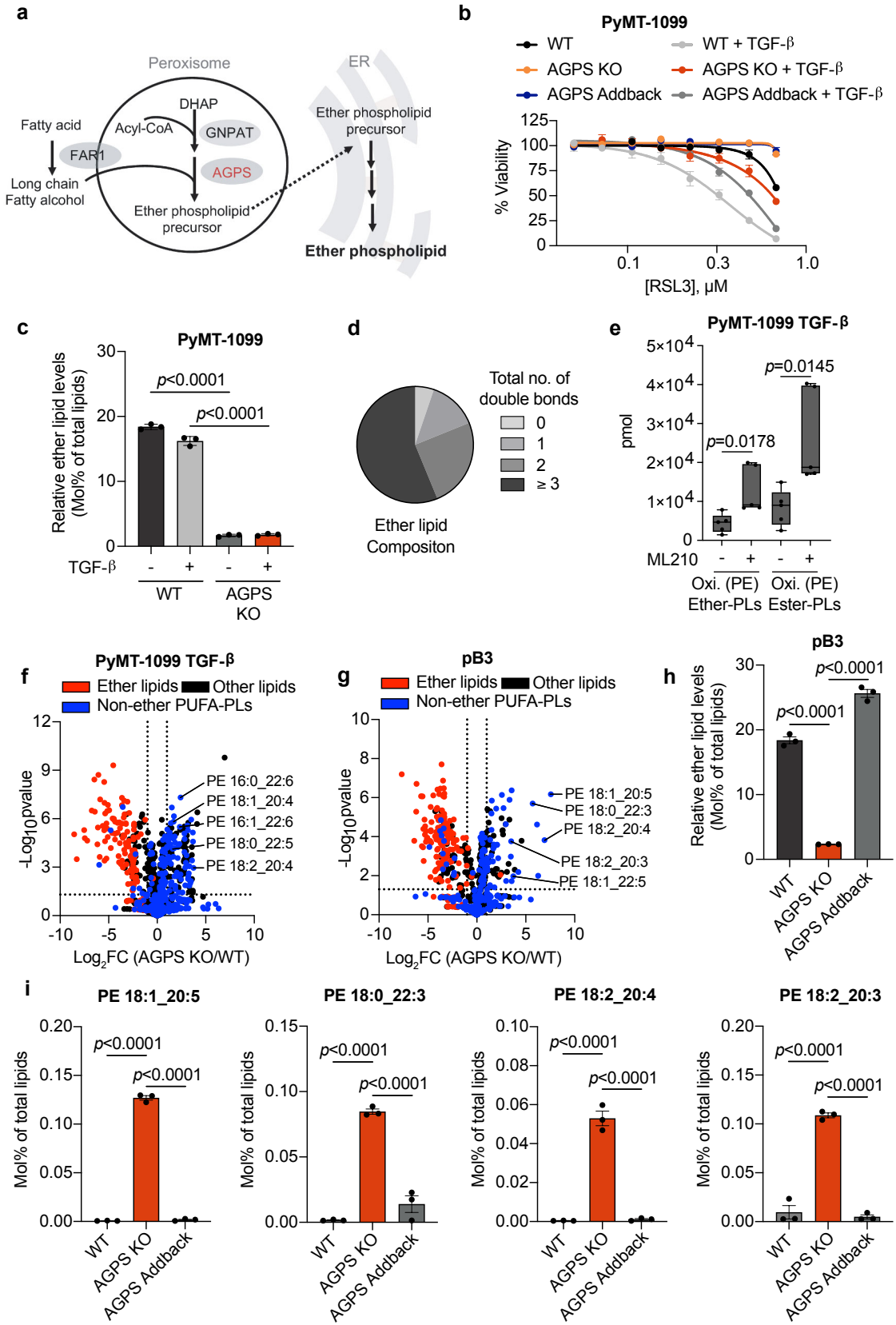
a
Peroxisome
ER
DHAP
Fatty acid
Acyl-CoA
GNPAT
FAR1
AGPS
Long chain
Fatty alcohol
Ether phospholipid
precursor
Ether phospholipid
precursor
Ether phospholipid
b
PyMT-1099
WT
AGPS KO
AGPS Addback
WT + TGF-β
AGPS KO + TGF-β
AGPS Addback + TGF-β
% Viability
[RSL3], μM
c
PyMT-1099
Relative ether lipid levels
(Mol% of total lipids)
p<0.0001
p<0.0001
TGF-β
WT
AGPS
KO
d
Total no. of
double bonds
0
1
2
≥ 3
Ether lipid
Compositon
e
PyMT-1099 TGF-β
pmol
p=0.0145
p=0.0178
ML210
Oxi. (PE)
Ether-PLs
Oxi. (PE)
Ester-PLs
f
PyMT-1099 TGF-β
Ether lipids
Other lipids
Non-ether PUFA-PLs
PE 16:0_22:6
PE 18:1_20:4
PE 16:1_22:6
PE 18:0_22:5
PE 18:2_20:4
Log2FC (AGPS KO/WT)
g
pB3
Ether lipids
Other lipids
Non-ether PUFA-PLs
PE 18:1_20:5
PE 18:0_22:3
PE 18:2_20:4
PE 18:2_20:3
PE 18:1_22:5
Log2FC (AGPS KO/WT)
h
pB3
Relative ether lipid levels
(Mol% of total lipids)
p<0.0001
p<0.0001
WT
AGPS KO
AGPS Addback
i
PE 18:1_20:5
PE 18:0_22:3
PE 18:2_20:4
PE 18:2_20:3
Mol% of total lipids
p<0.0001
p<0.0001
WT
AGPS KO
AGPS Addback

Fig. 2

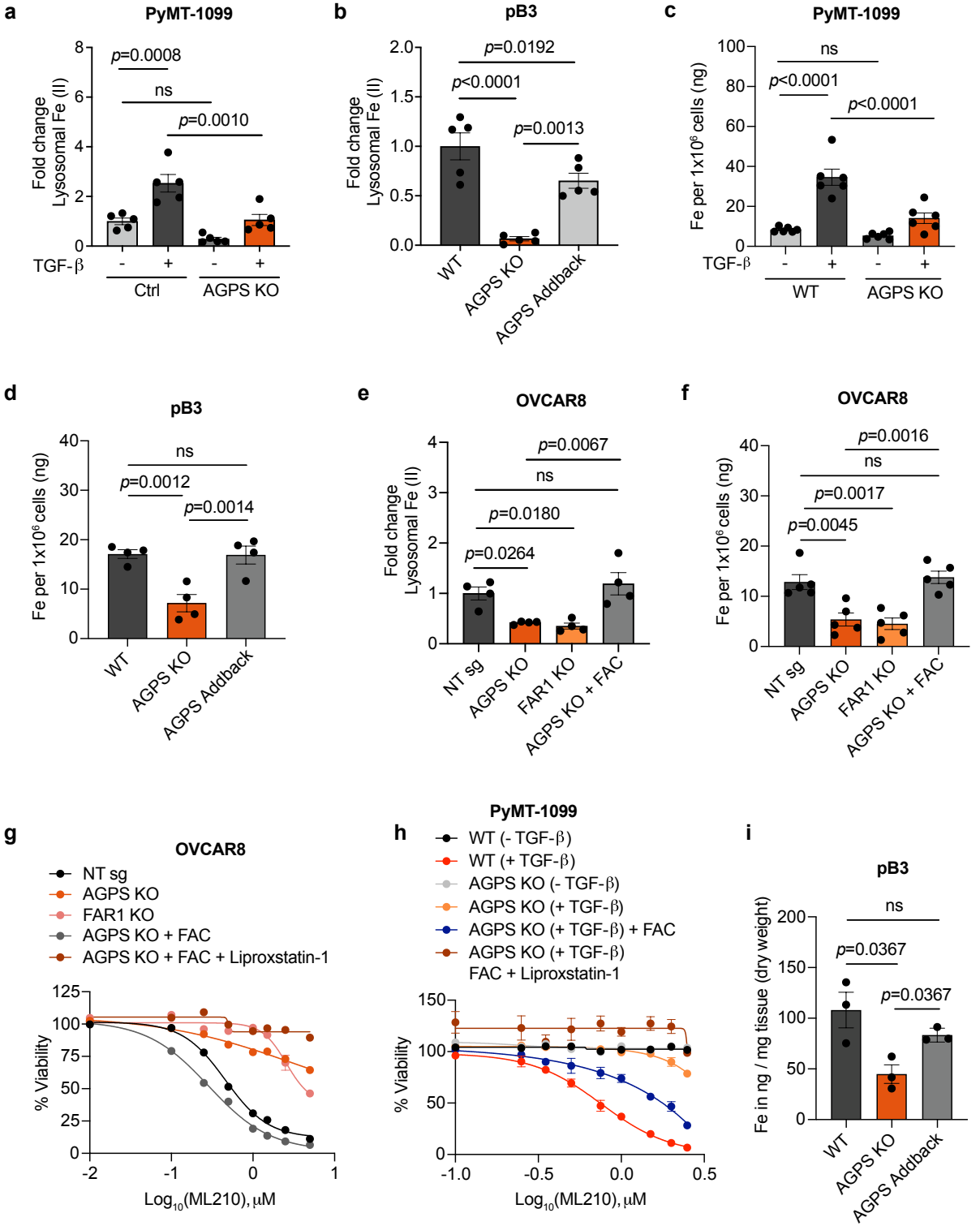
a
PyMT-1099
Fold change Lysosomal Fe (II)
p=0.0008
ns
p=0.0010
TGF-β
Ctrl
AGPS KO
b
pB3
Fold change Lysosomal Fe (II)
p=0.0192
p<0.0001
p=0.0013
WT
AGPS KO
AGPS Addback
c
PyMT-1099
Fe per 1x10^6 cells (ng)
ns
p<0.0001
p<0.0001
TGF-β
WT
AGPS KO
d
pB3
Fe per 1x10^6 cells (ng)
ns
p=0.0012
p=0.0014
WT
AGPS KO
AGPS Addback
e
OVCAR8
Fold change Lysosomal Fe (II)
p=0.0067
ns
p=0.0180
p=0.0264
NT sg
AGPS KO
FAR1 KO
AGPS KO + FAC
f
OVCAR8
Fe per 1x10^6 cells (ng)
p=0.0016
ns
p=0.0017
p=0.0045
NT sg
AGPS KO
FAR1 KO
AGPS KO + FAC
g
OVCAR8
NT sg
AGPS KO
FAR1 KO
AGPS KO + FAC
AGPS KO + FAC + Liproxstatin-1
% Viability
Log10(ML210), μM
h
PyMT-1099
WT (- TGF-β)
WT (+ TGF-β)
AGPS KO (- TGF-β)
AGPS KO (+ TGF-β)
AGPS KO (+ TGF-β) + FAC
AGPS KO (+ TGF-β) FAC + Liproxstatin-1
% Viability
Log10(ML210), μM
i
pB3
Fe in ng / mg tissue (dry weight)
ns
p=0.0367
p=0.0367
WT
AGPS KO
AGPS Addback

Fig. 3

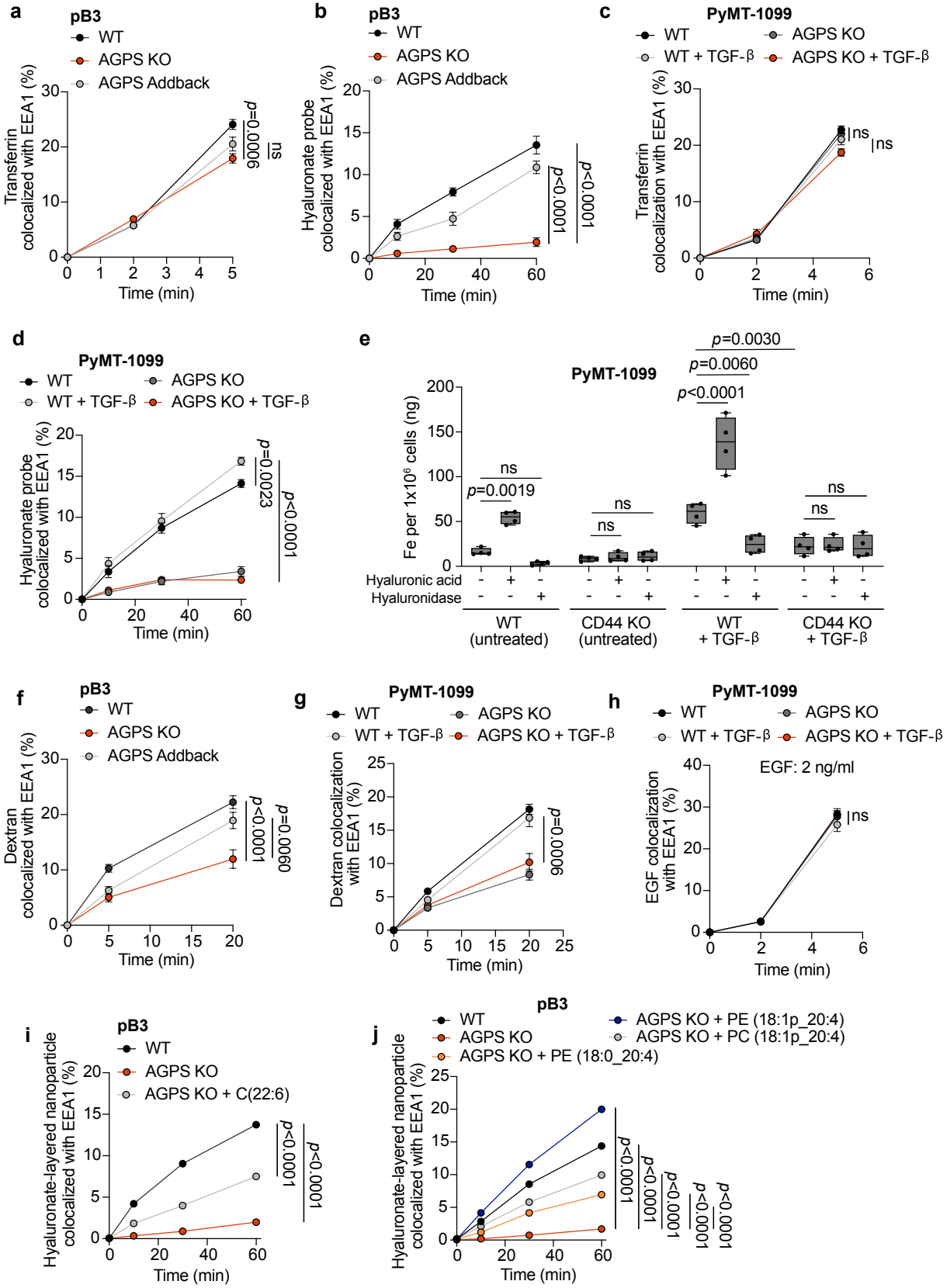
a
pB3
WT
AGPS KO
AGPS Addback
Transferrin colocalized with EEA1 (%)
Time (min)
p=0.0006
ns
b
pB3
WT
AGPS KO
AGPS Addback
Hyaluronate probe colocalized with EEA1 (%)
Time (min)
p<0.0001
p<0.0001
c
PyMT-1099
WT
WT + TGF-β
AGPS KO
AGPS KO + TGF-β
Transferrin colocalization with EEA1 (%)
Time (min)
ns
ns
d
PyMT-1099
WT
WT + TGF-β
AGPS KO
AGPS KO + TGF-β
Hyaluronate probe colocalized with EEA1 (%)
Time (min)
p=0.0023
p<0.0001
e
PyMT-1099
Fe per 1x10^6 cells (ng)
p=0.0030
p=0.0060
p<0.0001
ns
p=0.0019
ns
ns
ns
ns
Hyaluronic acid
Hyaluronidase
WT (untreated)
CD44 KO (untreated)
WT + TGF-β
CD44 KO + TGF-β
f
pB3
WT
AGPS KO
AGPS Addback
Dextran colocalized with EEA1 (%)
Time (min)
p<0.0001
p=0.0060
g
PyMT-1099
WT
WT + TGF-β
AGPS KO
AGPS KO + TGF-β
Dextran colocalization with EEA1 (%)
Time (min)
p=0.0006
h
PyMT-1099
WT
WT + TGF-β
AGPS KO
AGPS KO + TGF-β
EGF: 2 ng/ml
EGF colocalization with EEA1 (%)
Time (min)
ns
i
pB3
WT
AGPS KO
AGPS KO + C(22:6)
Hyaluronate-layered nanoparticle colocalized with EEA1 (%)
Time (min)
p<0.0001
p<0.0001
j
pB3
WT
AGPS KO
AGPS KO + PE (18:0_20:4)
AGPS KO + PE (18:1p_20:4)
AGPS KO + PC (18:1p_20:4)
Hyaluronate-layered nanoparticle colocalized with EEA1 (%)
Time (min)
p<0.0001
p<0.0001
p<0.0001
p<0.0001
p<0.0001

Fig. 4

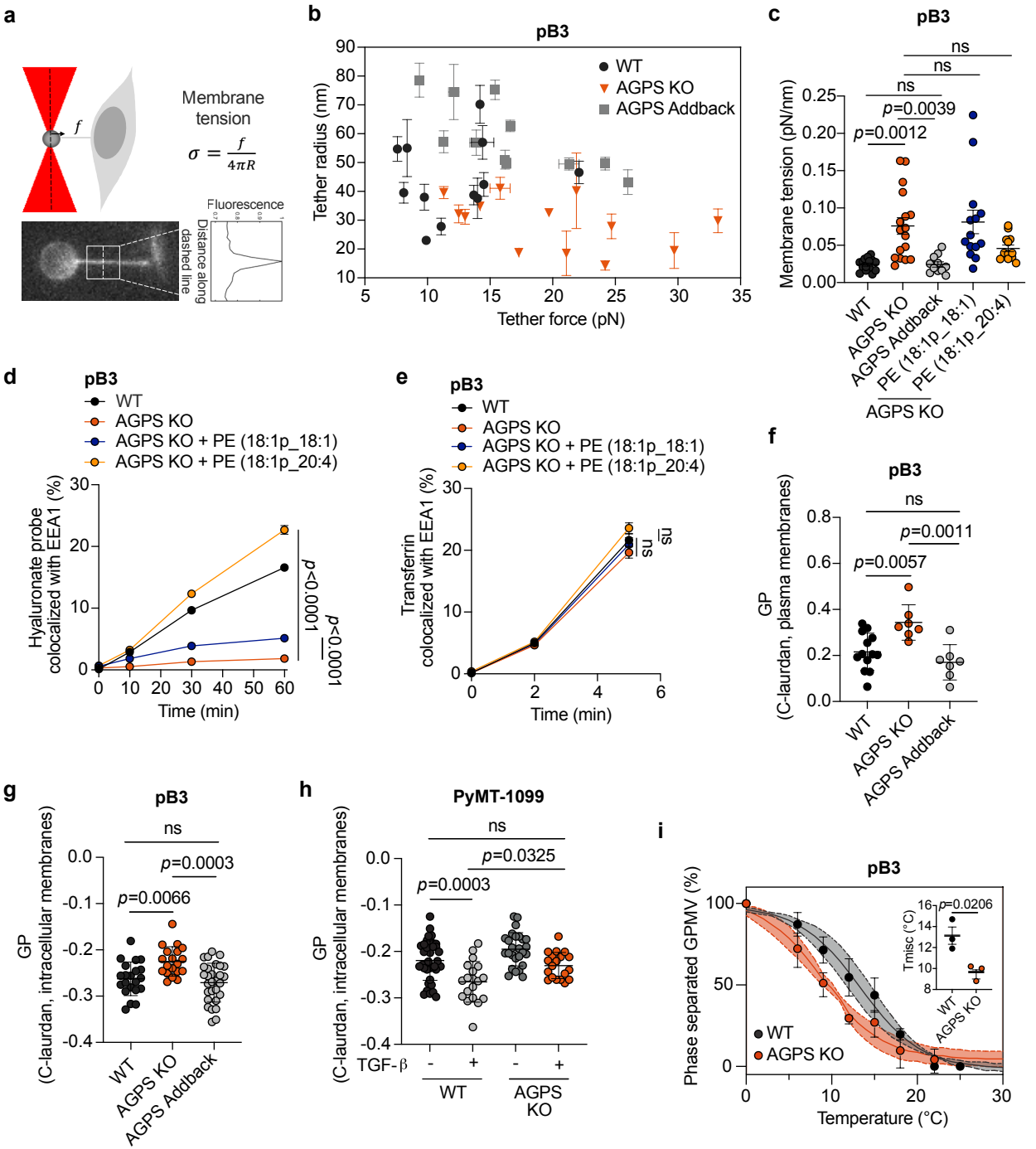
a
Membrane tension
$\sigma = \frac{f}{4\pi R}$
Fluorescence
Distance along dashed line
b
pB3
WT
AGPS KO
AGPS Addback
Tether radius (nm)
Tether force (pN)
c
pB3
Membrane tension (pN/nm)
p=0.0012
p=0.0039
ns
ns
ns
WT
AGPS KO
AGPS Addback
PE (18:1p_18:1)
PE (18:1p_20:4)
AGPS KO
d
pB3
WT
AGPS KO
AGPS KO + PE (18:1p_18:1)
AGPS KO + PE (18:1p_20:4)
Hyaluronate probe colocalized with EEA1 (%)
Time (min)
p<0.0001
p<0.0001
e
pB3
WT
AGPS KO
AGPS KO + PE (18:1p_18:1)
AGPS KO + PE (18:1p_20:4)
Transferrin colocalized with EEA1 (%)
Time (min)
ns
ns
ns
f
pB3
GP (C-laurdan, plasma membranes)
ns
p=0.0011
p=0.0057
WT
AGPS KO
AGPS Addback
g
pB3
GP (C-laurdan, intracellular membranes)
ns
p=0.0003
p=0.0066
WT
AGPS KO
AGPS Addback
h
PyMT-1099
GP (C-laurdan, intracellular membranes)
ns
p=0.0325
p=0.0003
TGF-β
-
+
-
+
WT
AGPS KO
i
pB3
Phase separated GPMV (%)
Temperature (°C)
WT
AGPS KO
Tmisc (°C)
p=0.0206
WT
AGPS KO

Fig. 5

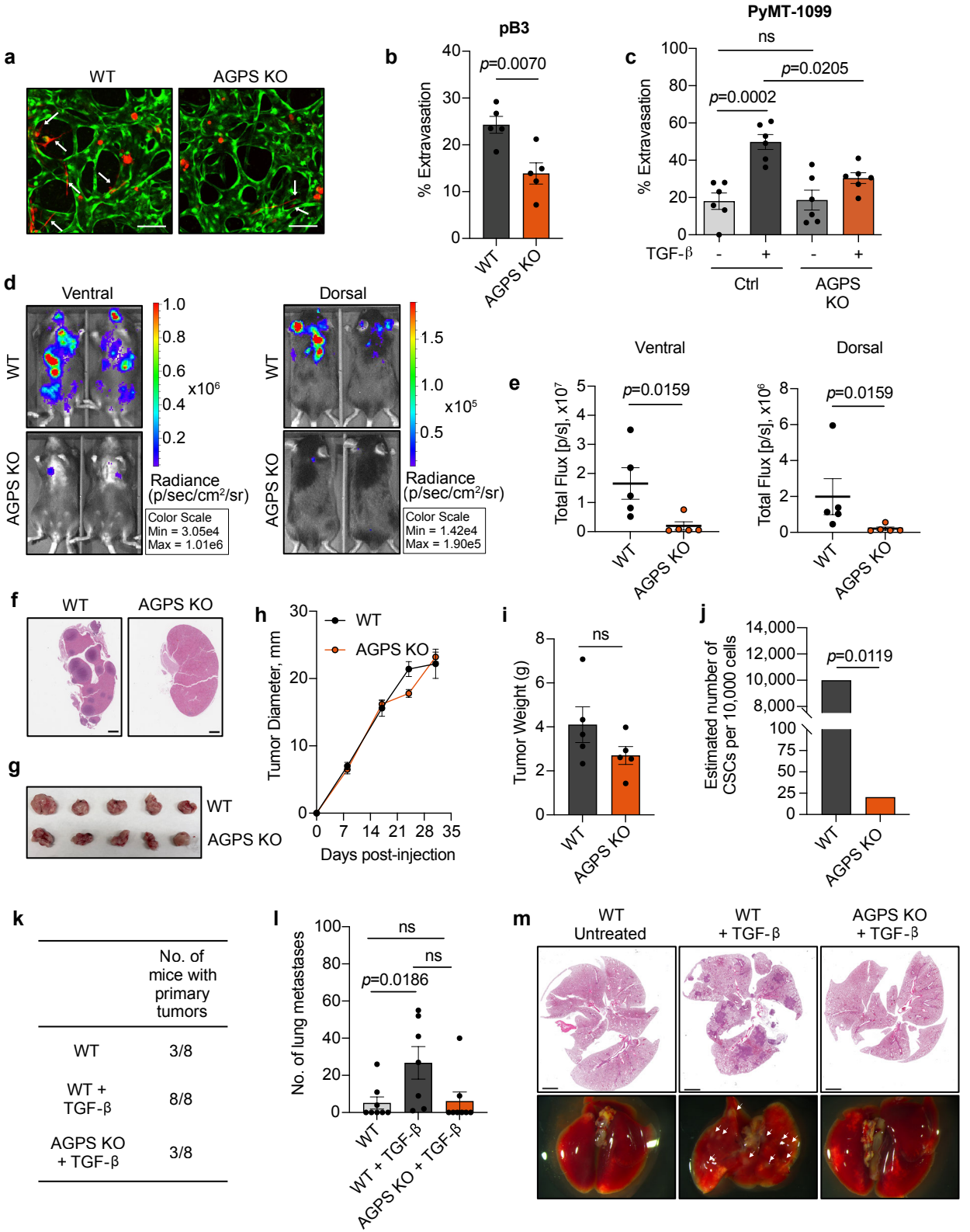
a
WT
AGPS KO
b
pB3
p=0.0070
% Extravasation
WT
AGPS KO
c
PyMT-1099
ns
p=0.0205
p=0.0002
% Extravasation
TGF-β
Ctrl
AGPS KO
d
Ventral
Dorsal
WT
AGPS KO
x10^6
x10^5
Radiance (p/sec/cm²/sr)
Color Scale Min = 3.05e4 Max = 1.01e6
Color Scale Min = 1.42e4 Max = 1.90e5
e
Ventral
Dorsal
p=0.0159
Total Flux [p/s], x10^7
Total Flux [p/s], x10^6
f
WT
AGPS KO
g
WT
AGPS KO
h
WT
AGPS KO
Tumor Diameter, mm
Days post-injection
i
ns
Tumor Weight (g)
j
p=0.0119
Estimated number of CSCs per 10,000 cells
k
No. of mice with primary tumors
WT 3/8
WT + TGF-β 8/8
AGPS KO + TGF-β 3/8
l
ns
ns
p=0.0186
No. of lung metastases
WT
WT + TGF-β
AGPS KO + TGF-β
m
WT Untreated
WT + TGF-β
AGPS KO + TGF-β

Extended Data Fig. 1

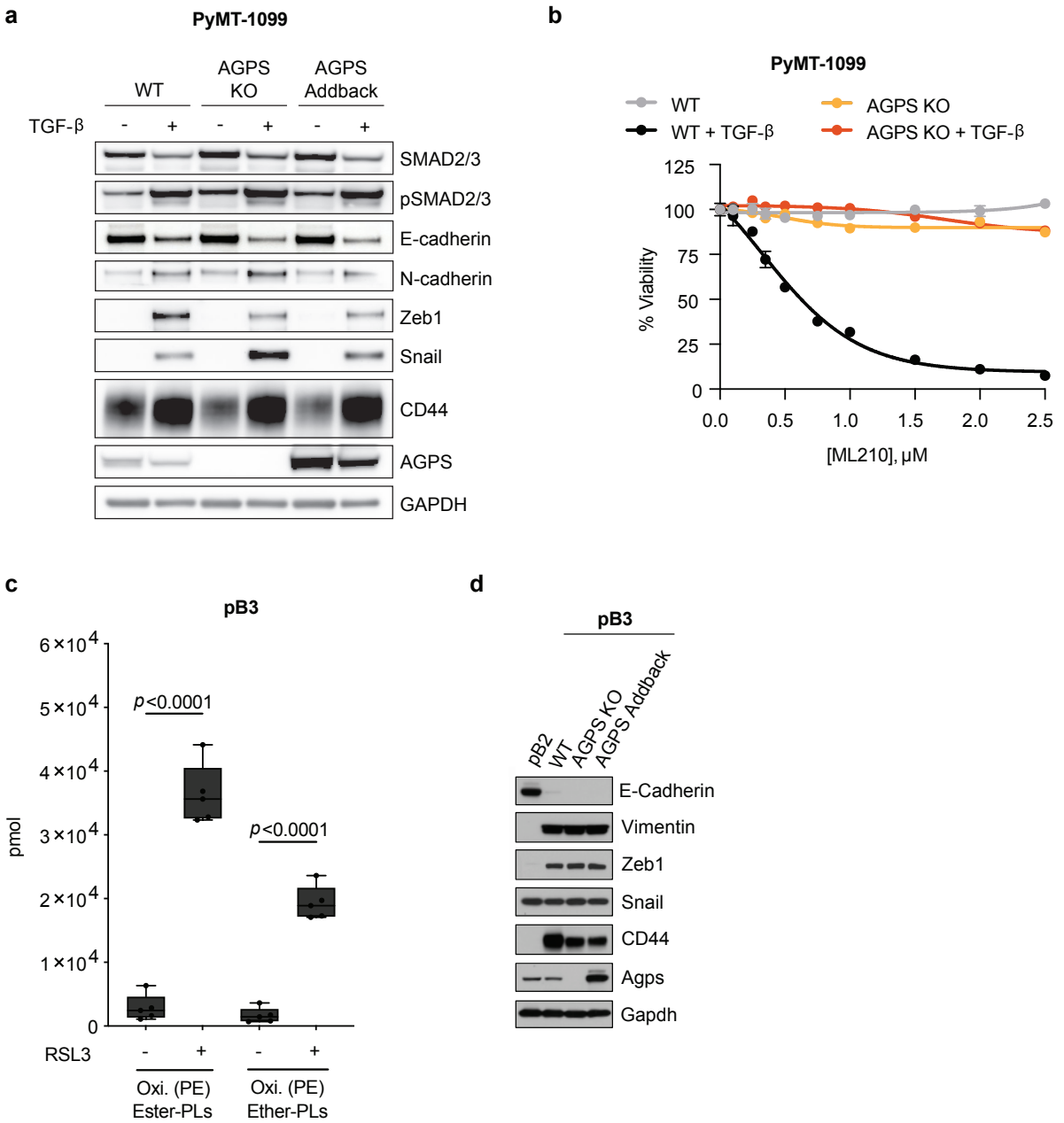

Extended Data Fig. 2

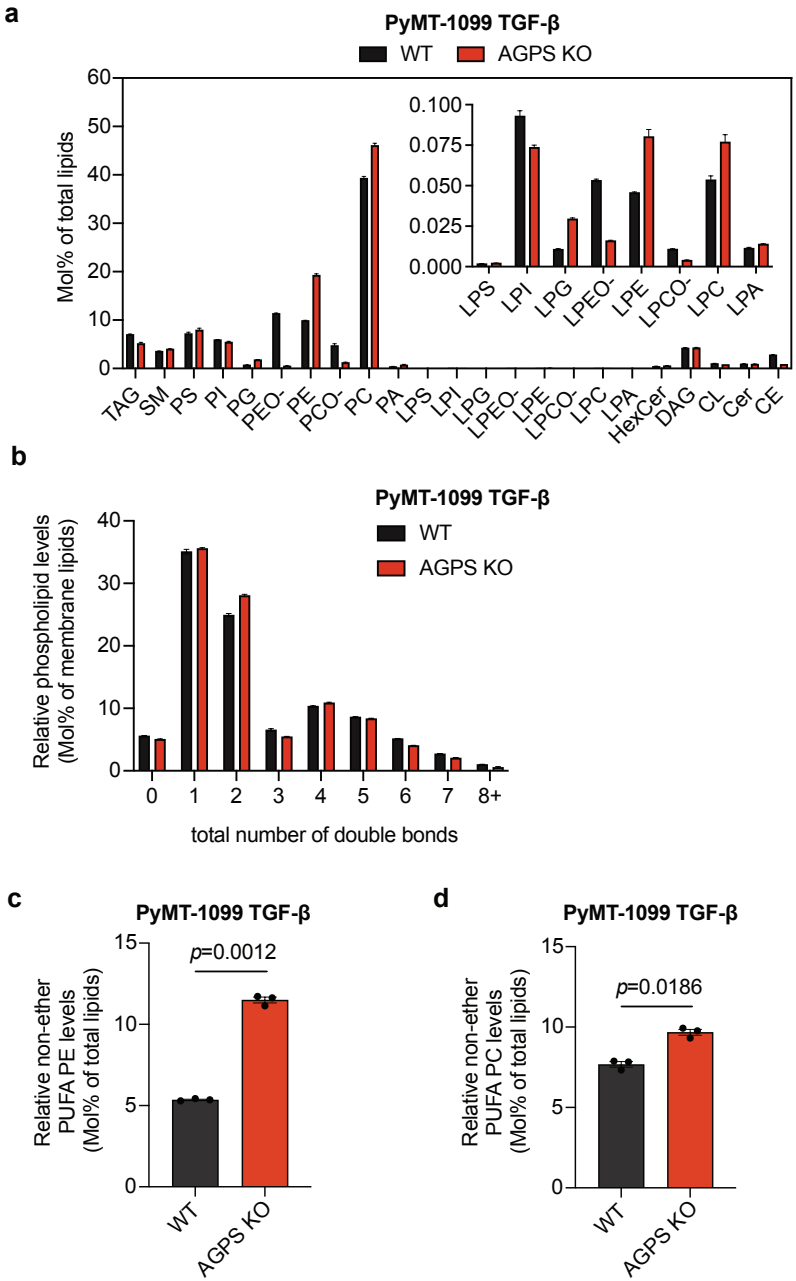

Extended Data Fig. 3

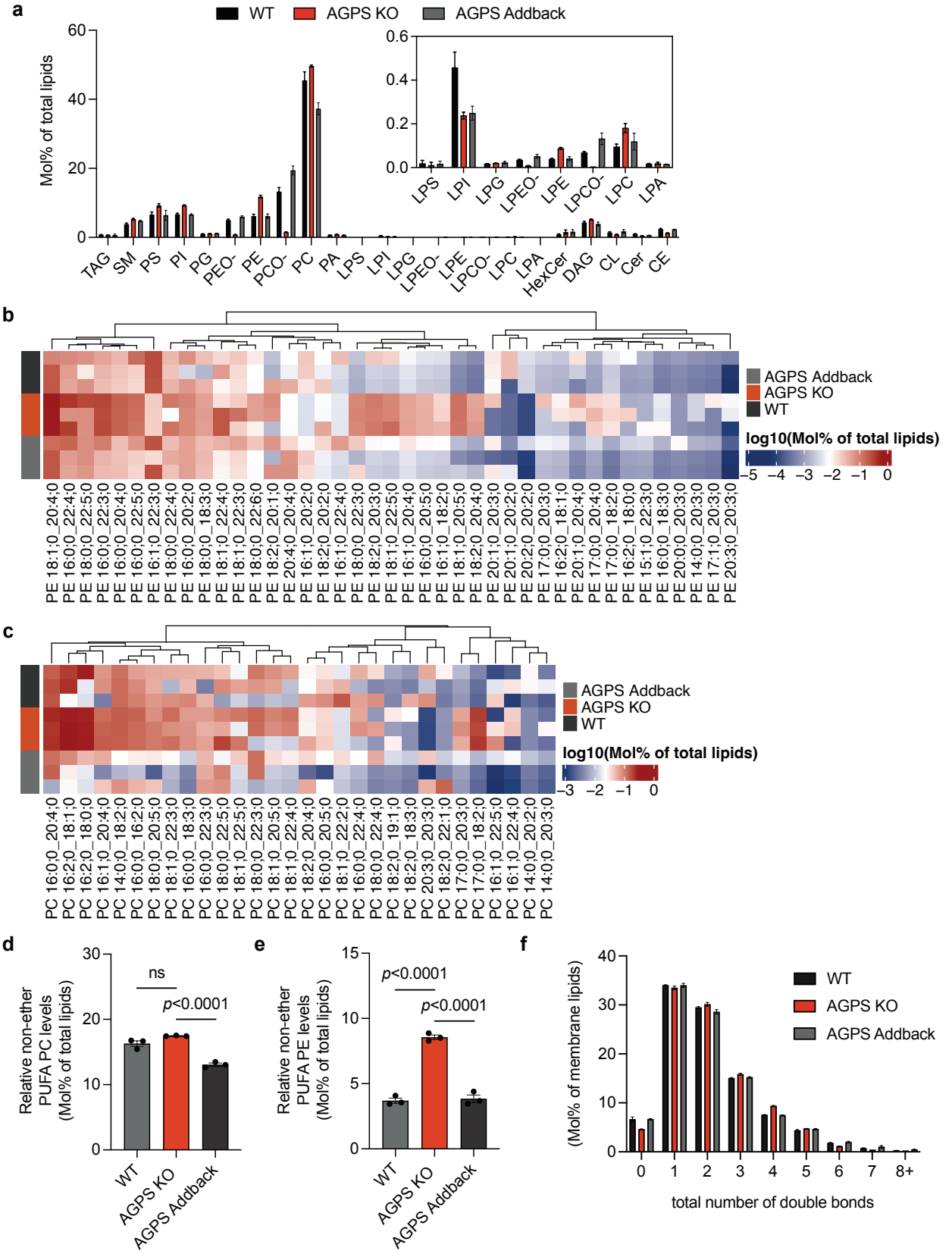

Extended Data Fig. 4

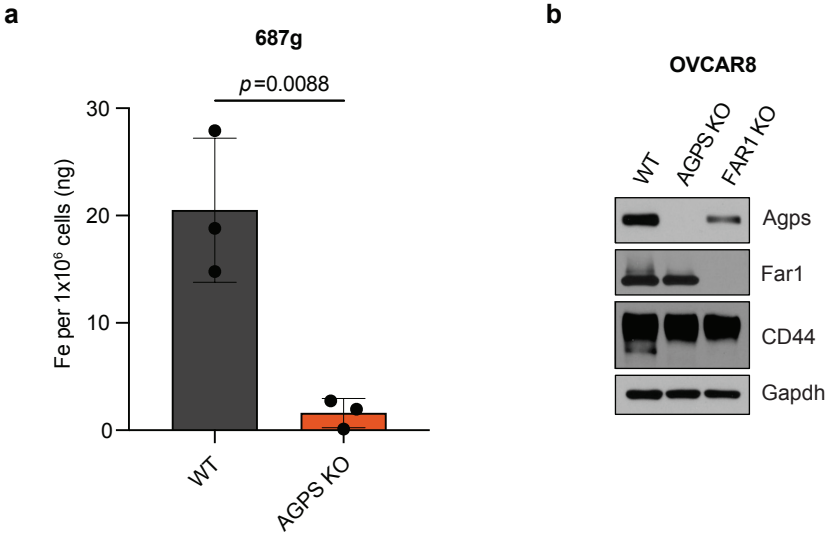

Extended Data Fig. 5

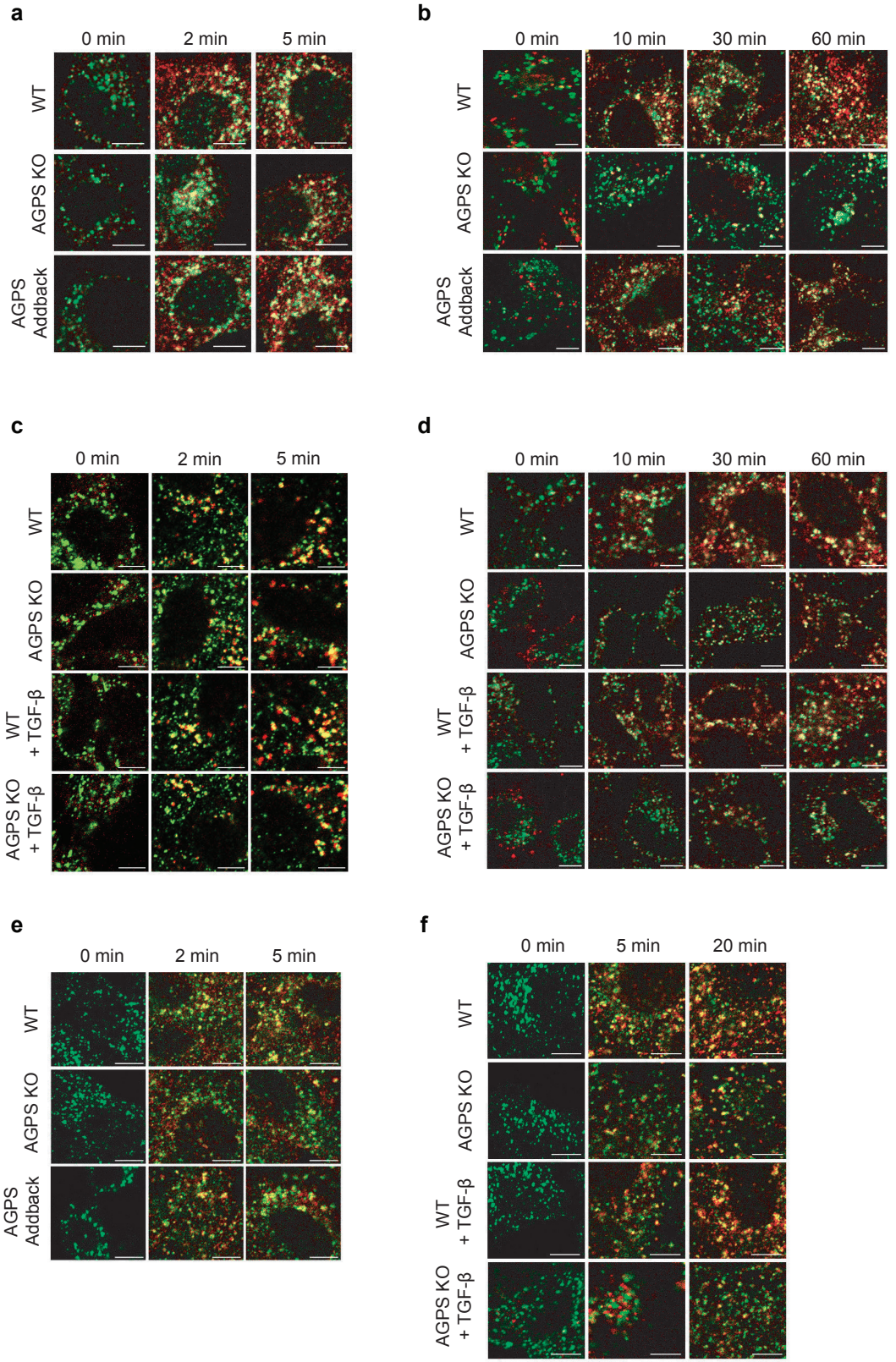

Extended Data Fig. 6

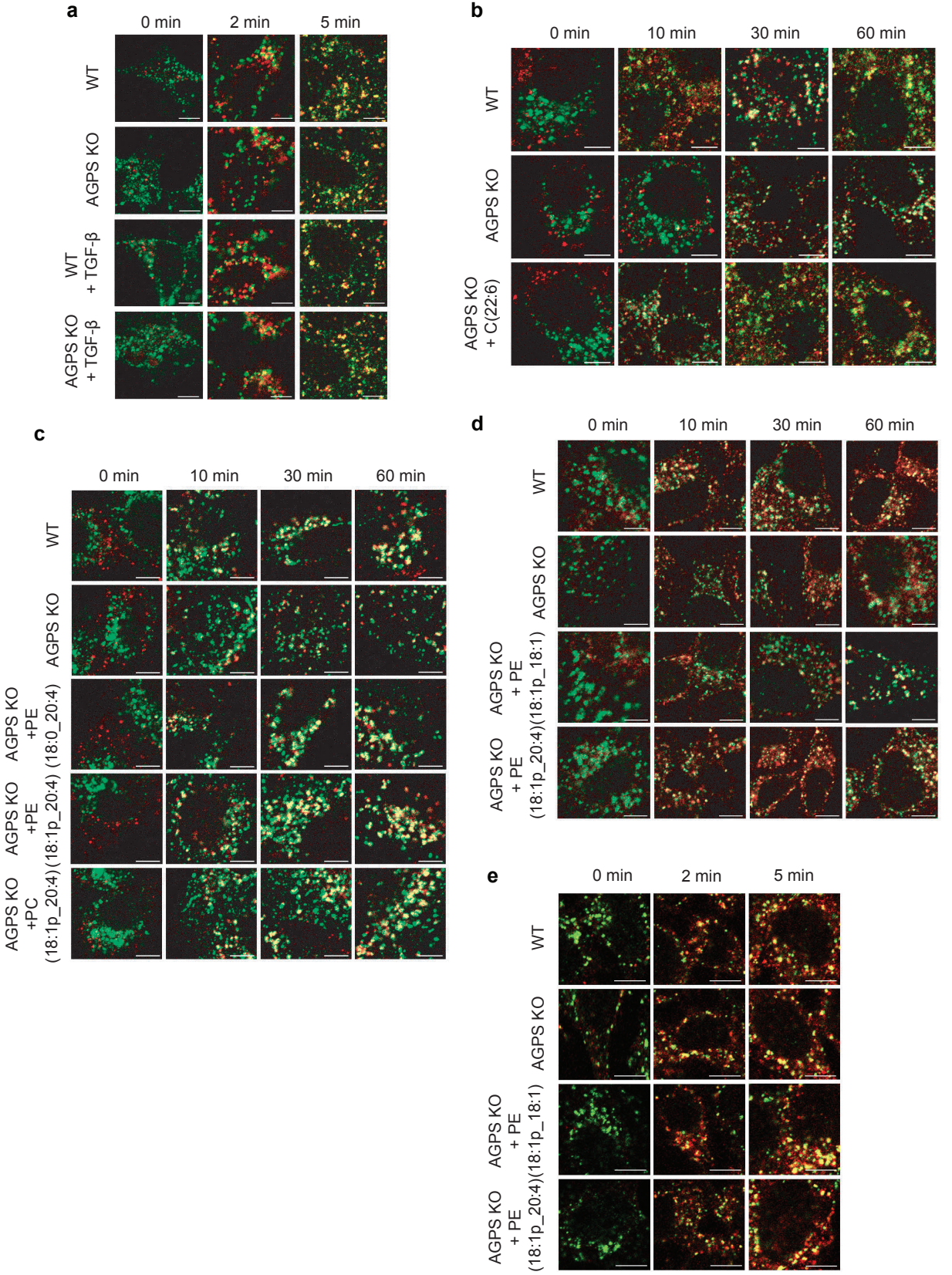

Extended Data Fig. 7

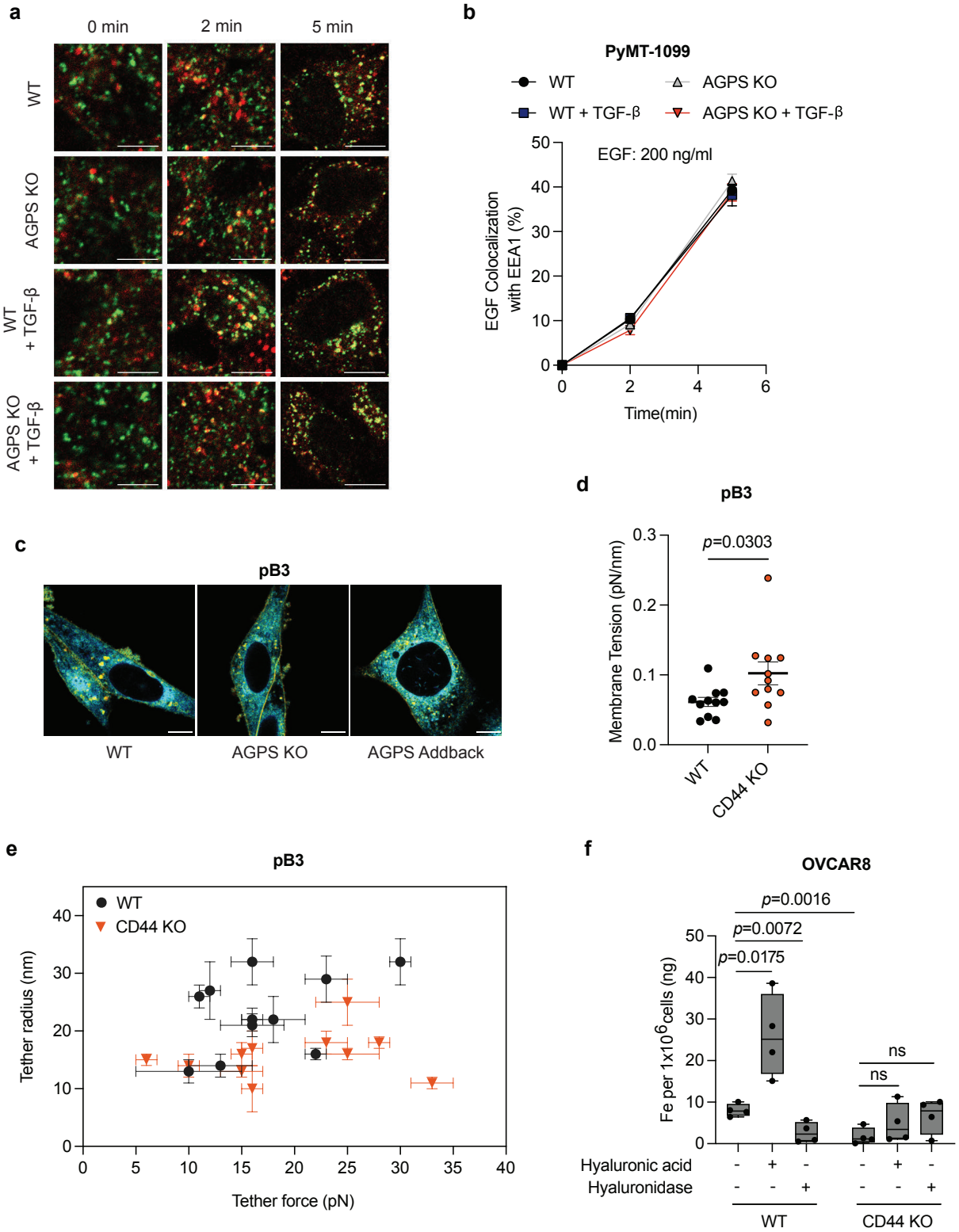

Extended Data Fig. 8

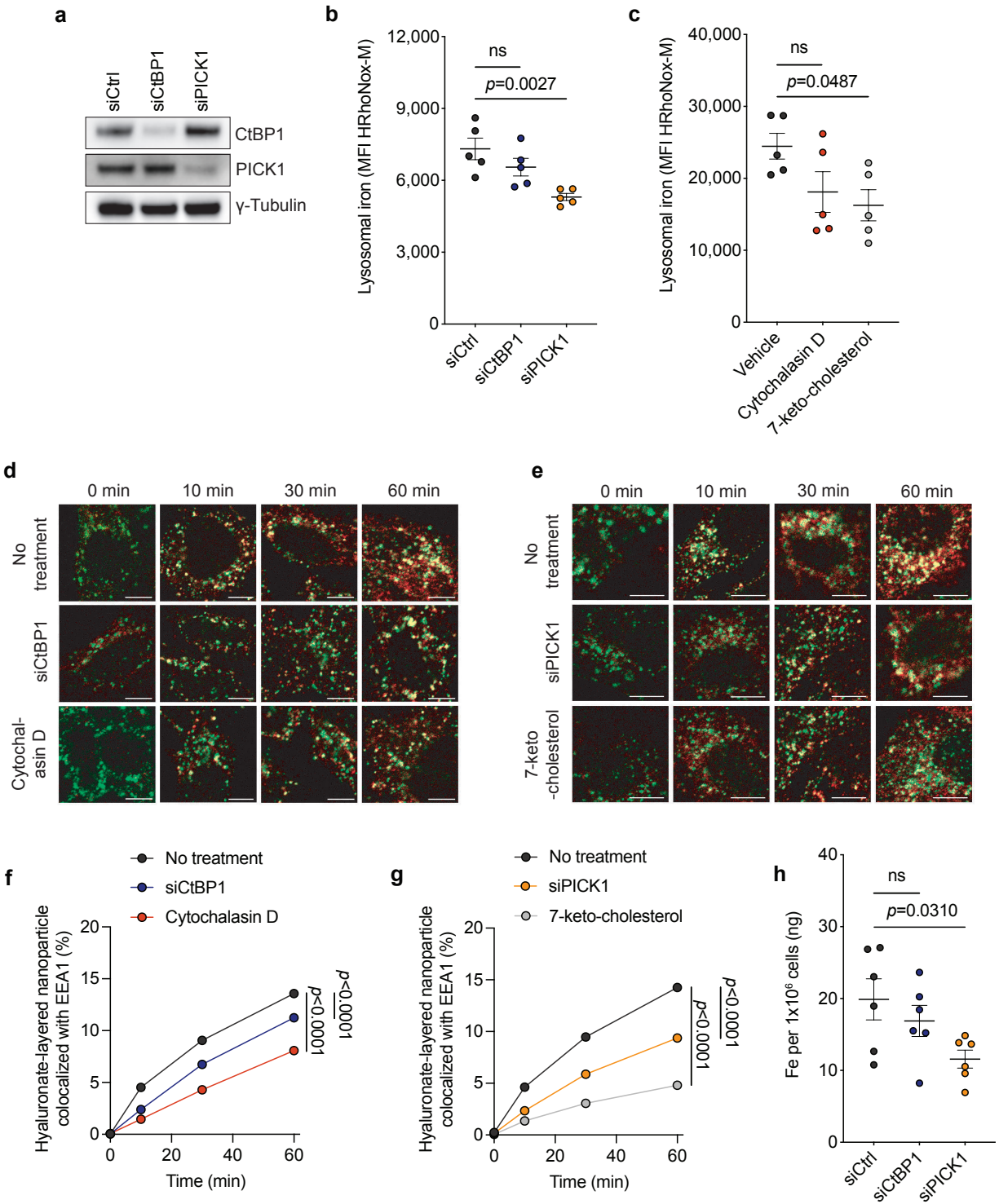

Extended Data Fig. 9

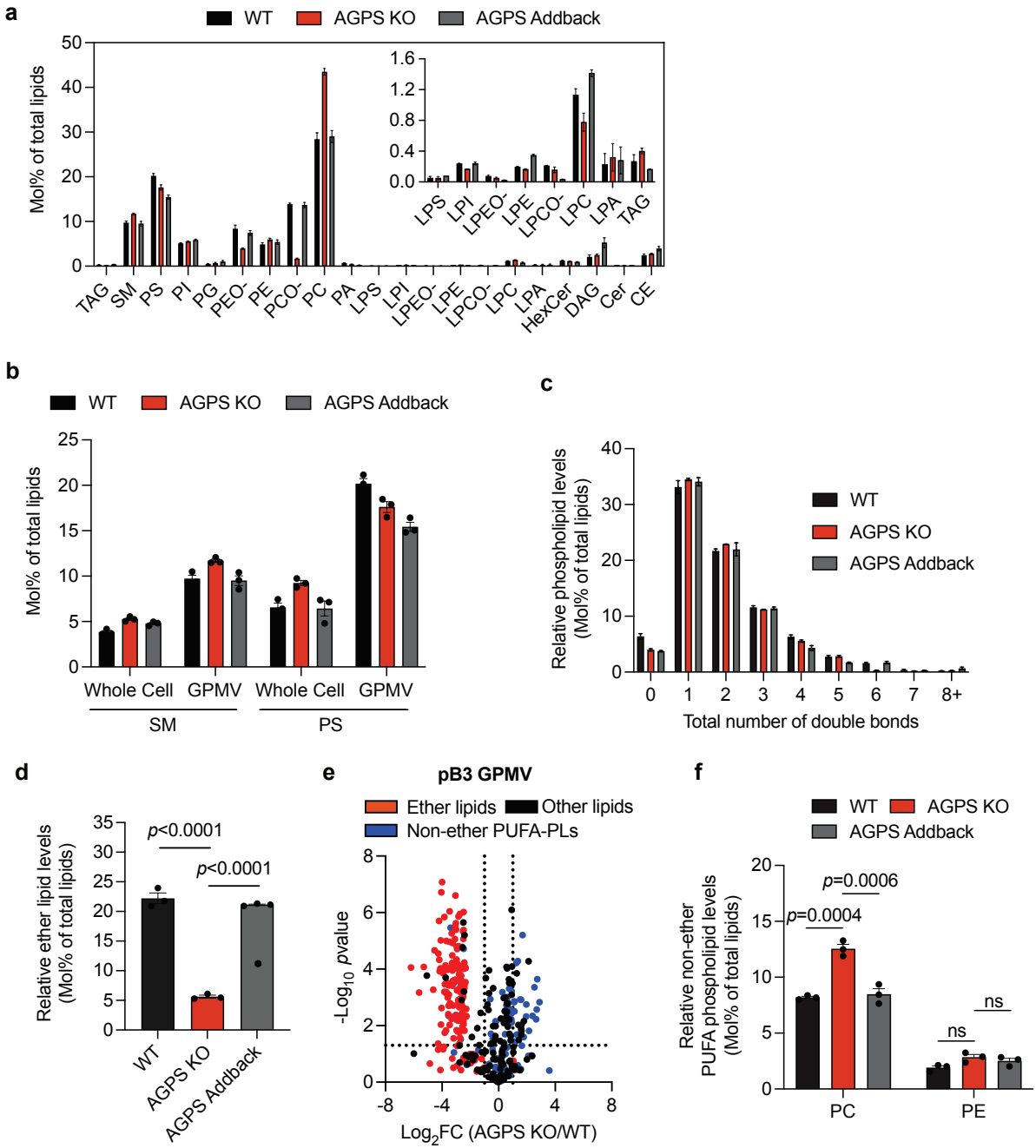

Extended Data Fig. 10

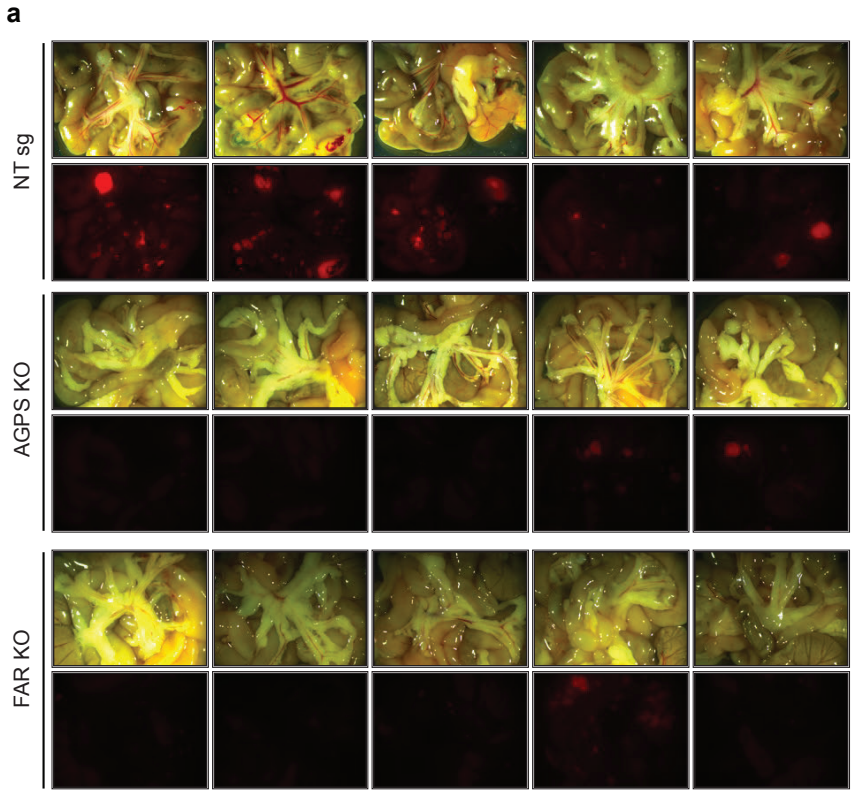

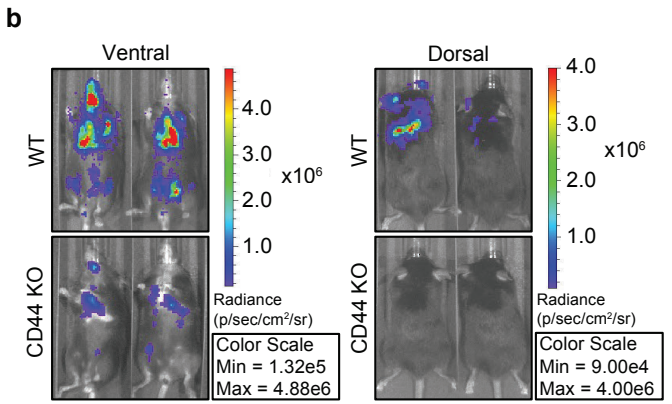

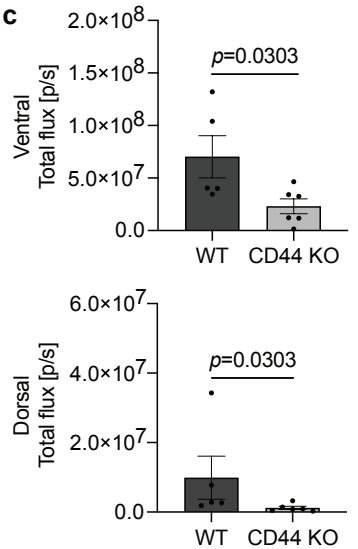

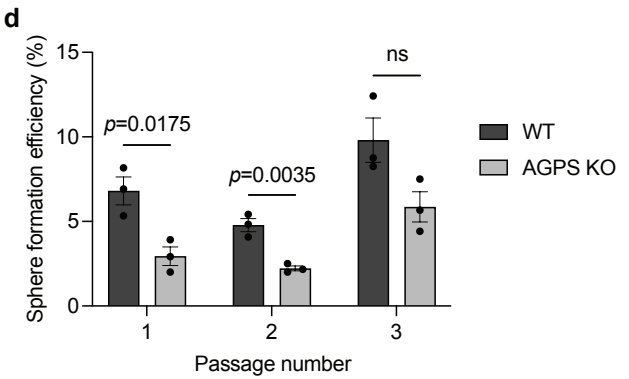

e

No. of cells implanted	100	1,000	10,000	100,000
WT	3/3	3/3	3/3	3/3
AGPS KO	0/3	3/3	3/3	3/3

Extended Data Fig. 11

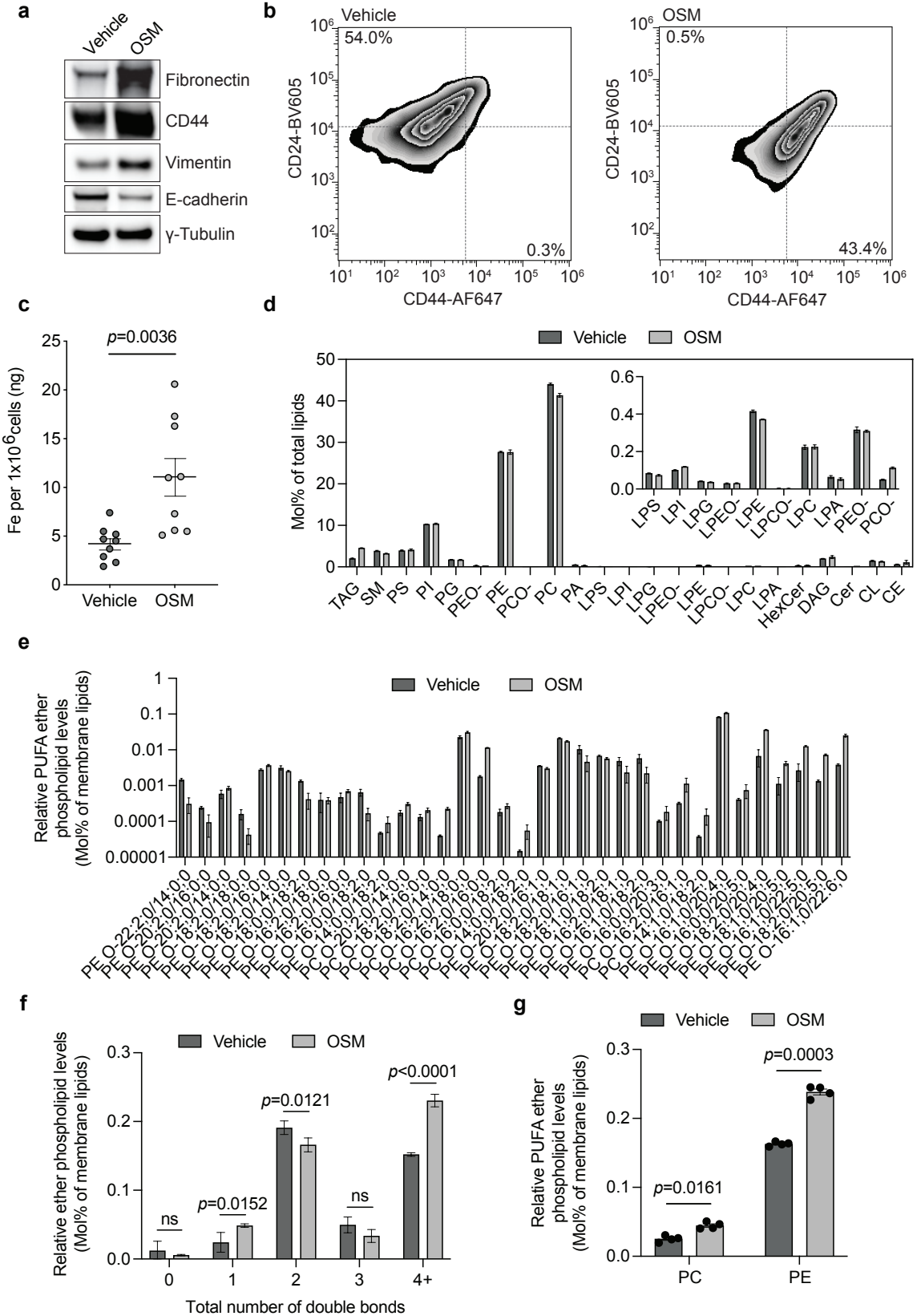
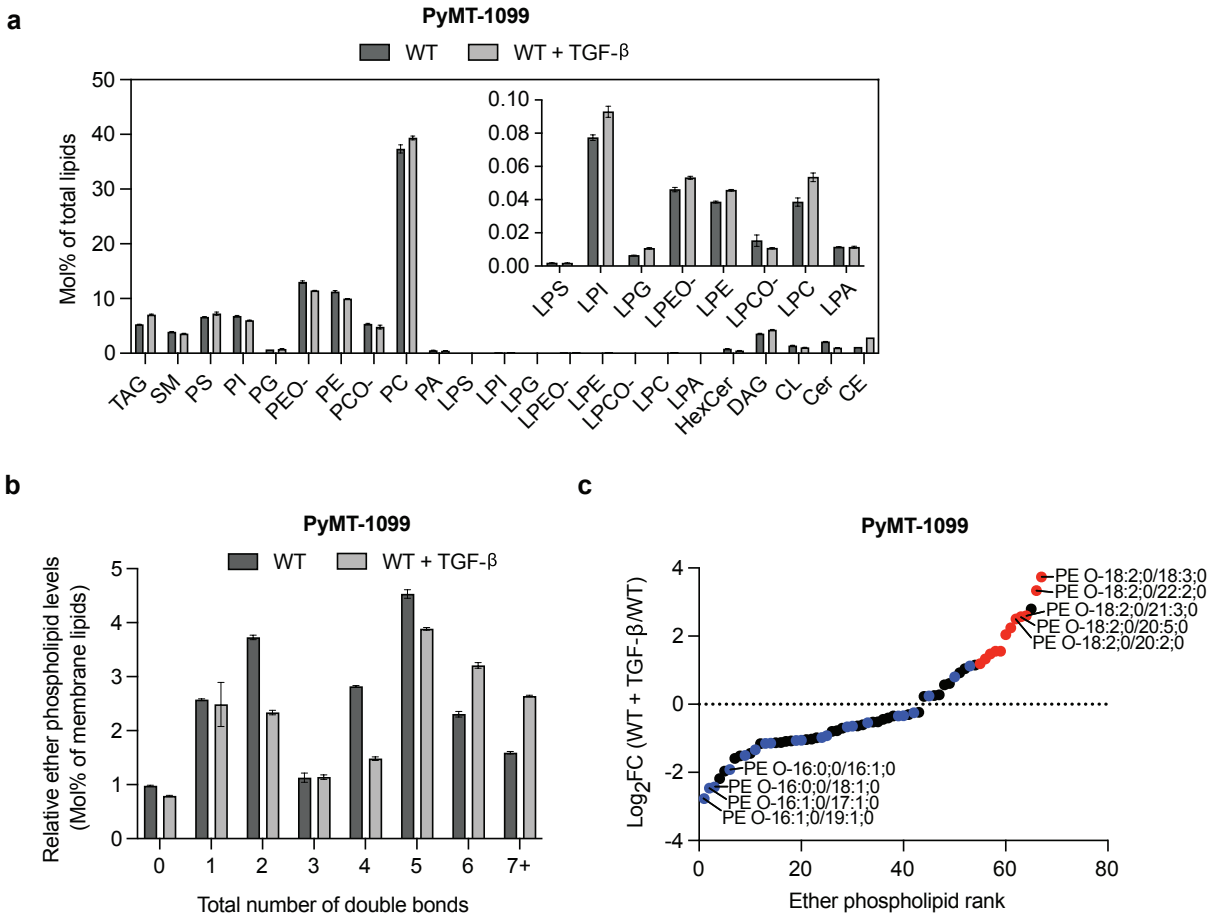
Extended Data Fig. 12